electronics

MDPI

Article

A Subwavelength Multiband Bandstop Metamaterial Reflector Using Double Interdigital Structure with Tri-Section Step-Impedance Technique for Gain Enhancement

Jessada Konpang [1], Prayoot Akkaraekthalin [2,*], Pongsathorn Chomtong [3] and Nutapong Somjit [4]

[1] Department of Electrical and Telecommunication Engineering, Faculty of Engineering, Rajamangala University of Technology Krungthep, Bangkok 10120, Thailand; jessada.k@mail.rmutk.ac.th
[2] Department of Electrical and Computer Engineering, Faculty of Engineering, King Mongkut's University of Technology North Bangkok, Bangkok 10140, Thailand
[3] Department of Teacher Training in Electrical Engineering, Faculty of Technical Education, King Mongkut's University of Technology North Bangkok, Bangkok 10140, Thailand; pongsathornc@kmutnb.ac.th
[4] School of Electronic and Electrical Engineering, University of Leeds, Leeds LS2 9JT, UK; n.somjit@leeds.ac.uk
* Correspondence: prayoot.a@eng.kmutnb.ac.th

Abstract

This paper presents a subwavelength multiband bandstop metamaterial reflector for enhancing antenna gain beyond what is achieved by conventional metallic reflectors. The unit cell was designed to generate multiband stopbands at three frequencies: the first at 1.8 GHz, the second at 2.6 GHz, and the third at 3.5 GHz. The design was implemented on a low-cost FR-4 printed circuit board with a simple design and compact size. The unit-cell structure included a transmission line configuration using the tri-section step-impedance technique, combined with a capacitive load at the end of the transmission line via a double interdigital structure. The structure could control the first, second, and third resonance frequencies to occur at the desired bands and ensured independent resonances. The double interdigital capacitive load significantly increased capacitive loading, generating a strong slow-wave effect along the transmission line structure, exceeding that achieved with conventional capacitive loading techniques. As a result, the transmission line size of the unit cell was drastically reduced from the conventional $\lambda/2$ to $\lambda/16$. To achieve metamaterial characteristics, the unit cell was modified to exhibit negative permittivity (ENG) for enhanced reflection compared to conventional materials and positive permeability. This was accomplished by adding a rod (ROD) structure behind the main structure using the tri-section step-impedance technique. This configuration generated left-handed current on the structure, resulting in negative permittivity values at all three resonance frequencies. An array of 14 $\times$ 14 unit cells was fabricated to form the metamaterial reflector with an overall size of 148 mm $\times$ 161.7 mm, which is very compact. The performance was evaluated by placing a single-frequency resonant dipole antenna, operating at the same resonance frequency as the reflector, in front of the reflector along the X-axis plane. The antenna gain increased from approximately 2 dB at all frequencies to about 8 dB. The radiation pattern exhibited directional radiation at 0 degrees. The measured results of frequency responses and antenna gains were close to the simulated results. With superior characteristics and compact size, the proposed metamaterial reflector can be applied for multiband 5G and other modern antenna systems.

Keywords: metamaterial; double interdigital; capacitive load; tri-section step-impedance; multiband bandstop reflector

Check for updates

Received: 22 July 2026
Revised: 17 August 2026
Accepted: 19 August 2026
Published: 22 August 2026

Copyright: © 2026 by the authors. Licensee MDPI, Basel, Switzerland. This article is an open access article distributed under the terms and conditions of the Creative Commons Attribution (CC BY) license.

1. Introduction

At present, modern wireless communication technology is developing rapidly and continuously to support the increasing and diverse demands of users. All communication devices become smaller, operate on multiple frequency bands, support very high data rates, and handle larger data volumes. Researchers have continuously investigated and developed various techniques to achieve these objectives. One of the essential components of any wireless communication system is the antenna. Therefore, antenna development has become widespread, focusing on size reduction, suitable bandwidths to avoid interference from adjacent frequencies, multiband operation, and gain enhancement to increase communication distance. However, despite these advancements, several limitations still exist. Although modern antennas support multiple frequency bands and compact sizes at higher resonance frequencies, the radiation pattern often exhibits main-lobe splitting. This phenomenon prevents effective control of the radiation angle and direction. Furthermore, with gain enhancement techniques that can be used with some types of reflectors, the main-lobe splitting still occurs. In addition, the spacing between the antenna and the reflector remains approximately $\lambda/4$ to achieve phase reinforcement after reflection. This spacing limits antenna-profile reduction. To overcome these challenges, researchers have introduced metamaterials applied for antenna design. Metamaterials exhibit electromagnetic properties that differ from natural materials. In conventional materials, permittivity and permeability are both positive. In contrast, metamaterials can exhibit negative permittivity, negative permeability, or both due to left-handed current behavior, often achieved using rod (ROD) structures. When permittivity becomes negative, known as epsilon-negative (ENG), the material enhances electromagnetic wave reflection more effectively than conventional materials [1–6]. When permeability becomes negative, known as mu negative (MNG), the material improves electromagnetic wave transmission compared to conventional materials [7–10]. If both parameters become negative, referred to as a double negative (DNG) material, the material supports both strong transmission and reflection depending on the design, although the design process becomes highly complex [11–15]. In addition, near-zero electromagnetic metamaterials have been investigated for phase and radiation-direction control in antenna applications [16–19], which enable effective phase and radiation direction control for antenna applications. Based on these properties, metamaterials have been widely applied in wireless communication systems. For example, electromagnetic bandgap (EBG) structures suppress surface waves and allow only propagating waves, thereby improving reflection performance compared to conventional materials [20–24]. Frequency-selective surfaces (FSSs) allow transmission only within desired frequency bands [25,26]. Metamaterial technology has continuously evolved to support multiband operation [7,27–29], miniaturized unit-cell designs [10,30–32], and even terahertz-frequency metamaterials for ultra-high-frequency applications to increase bandwidth capacity. Previous studies showed that smaller unit-cell sizes with a larger number of cells improved the ability to control effective electromagnetic parameters compared to larger unit cells. However, many researchers attempted to reduce the unit-cell size below $\lambda/2$; the structures remained relatively large and could not precisely control electromagnetic characteristics at higher frequencies as desired. Moreover, when applied to antenna gain enhancement, the resulting antenna gain is still low.

In this research article, we present the design of a subwavelength multiband bandstop metamaterial reflector. The structure is designed on an FR-4 printed circuit board with permittivity = 4.4, substrate height = 1.6 mm, copper thickness = 0.035 mm, and loss tangent = 0.02. The unit cell is designed to operate as a multiband bandstop resonator based on bandstop resonator concepts widely studied in previous works [33–38]. The first resonance frequency occurs at 1.8 GHz, while the second and third resonance frequencies

are controlled to resonate at 2.6 GHz and 3.5 GHz, respectively. The design employs a double interdigital capacitive load connected at the end of the transmission line together with a tri-section step-impedance transmission line technique [39,40]. Previous studies have used capacitive loading techniques to control resonance behavior [41–46]. The double interdigital technique in this work provides a significantly higher capacitive load than conventional capacitive loading methods. As a result, the slow-wave effect increases the electrical length for a fixed physical length, thereby shifting the resonances toward lower frequencies. To maintain resonance at the desired original frequency band, the physical length of the transmission line is reduced to compensate for the increased electrical length. Consequently, the overall transmission line structure becomes significantly smaller. Also, increasing the capacitive load further enhances the size reduction in the transmission line. In addition, the resonance frequencies can be tuned by adjusting the capacitive load. However, capacitive loading alone does not provide precise control of the resonance frequencies. Therefore, the tri-section step-impedance technique is applied because it controls resonance through impedance differences along the transmission line. By combining these two techniques, the unit-cell size is significantly reduced, resulting in a very compact size. Then, a rod (ROD) structure designed using the tri-section step-impedance technique is added to ensure left-handed current generation at all three resonance frequencies. At the three resonance frequencies, the effective permittivity exhibits epsilon-negative (ENG) behavior, while the effective permeability demonstrates positive permeability characteristics. These properties enhance electromagnetic wave reflection compared with conventional materials. The proposed unit cell is then arranged in an array to form a metamaterial reflector applied for antenna applications. The design process is straightforward and cost-effective. Detailed design methodology is described in the following section.

2. Design of Multiband Bandstop Metamaterial Reflector

This section presents the design of the multiband bandstop metamaterial reflector, which consists of two main parts. The first part is the multiband bandstop metamaterial unit-cell design, which explains the design of the unit-cell structure for controlling multiband stopband resonance frequencies while achieving negative permittivity and positive permeability characteristics at the resonance frequencies, along with significant size reduction. The second part is the metamaterial reflector design, which presents the array configuration of the metamaterial unit cells to form the reflector and describes the integration of a single-frequency dipole antenna to evaluate the antenna gain enhancement performance.

2.1. Design of Multiband Bandstop Metamaterial Unit Cell

The multiband metamaterial unit cell presented in this section is designed on an FR-4 printed circuit board. The structure is based on a transmission line configuration with an interdigital capacitive technique [41–44]. This connection creates a high capacitive load, producing a slow-wave effect along the transmission line. As widely reported in previous studies, this effect causes the electrical length to differ from the physical length of the transmission line, enabling size reduction from approximately $\lambda/2$ to about $\lambda/8$ [41,42]. In addition, the second resonance frequency can be controlled so that the bandpass resonance occurs within the desired frequency range. This capability allows the resonator size to be reduced while simultaneously controlling the second resonance frequency by increasing or decreasing the capacitive load between the interdigital fingers. However, the results obtained from this technique still mainly involve controlling the resonance to produce a band-pass response at the desired frequencies. Such an approach typically allows control of only two resonance frequencies, and the adjustment of the capacitive load is also limited by the physical structure of the interdigital fingers, since the number of fingers can only be

increased up to a certain level. Consequently, the resonator size cannot be reduced beyond $\lambda/8$. Therefore, the unit cell proposed in this work aims to improve the performance and overcome the limitations mentioned above. The design introduces a multibandstop resonance frequency, in which the insertion loss coefficient (S_{21}) becomes negative while the return loss coefficient (S_{11}) approaches near zero at the resonance frequencies. The proposed structure is designed such that the first resonance frequency occurs at 1.8 GHz, while the second and third resonance frequencies are controlled to resonate at 2.6 GHz and 3.5 GHz, respectively. These resonance frequencies correspond to frequency bands used in 5G wireless communication systems. The unit cell is designed to achieve a size smaller than $\lambda/8$, without structural limitations for increasing the capacitive load, while enabling three quasi-independently tuned resonance frequencies and providing stronger reflection characteristics than conventional natural materials. The design process begins with a transmission line structure whose signal line ends are connected using a double interdigital technique. This configuration introduces an inner interdigital structure within the interdigital fingers, significantly increasing the capacitive load and simultaneously enhancing the slow-wave effect in the transmission line.

As a result, the electrical length and the physical length differ significantly. The slow-wave effect causes the physical length to remain constant while the electrical length decreases significantly, which is equivalent to an increase in the effective physical length of the transmission line [43,44]. Consequently, the first, second, and third resonance frequencies shift toward lower frequencies. To restore the first resonance frequency to its original position, the physical length must be reduced to match the electrical length. This process significantly reduces the physical size of the transmission line, allowing the structure to be reduced from approximately $\lambda/2$ to $\lambda/16$, which results in a much smaller unit-cell structure. However, the second and third resonance frequencies cannot yet be precisely controlled to occur exactly at the desired frequencies. Although the capacitive load helps control the resonance behavior to some extent, it cannot precisely tune both resonance frequencies to the required bands.

Therefore, to improve the precision of resonance control, the tri-section step-impedance technique is applied to the transmission line structure [39,40]. The difference between impedance values (Z) in each section enables fine-tuning of the second and third resonance frequencies, allowing them to shift to the desired frequency bands. With this approach, the proposed unit cell can quasi-independently tune and control three resonance frequencies. However, although the three bandstop resonance frequencies are successfully controlled, the simulated results show that the permittivity (ε_r) and permeability (μ_r) remain positive even when the insertion loss coefficient (S_{21}) becomes negative at the resonance bands [16–19]. Therefore, to achieve negative effective parameters, a rod (ROD) structure is introduced on the backside of the unit cell to generate left-handed current circulation on the structure [11–15]. This current behavior causes the effective electromagnetic parameters to become negative. Nevertheless, a conventional ROD structure implemented as a standard transmission line typically produces left-handed current only at the first resonance frequency. Higher-order harmonic resonances, including the second and third resonance frequencies, do not produce the required current circulation. As a result, ε_r and μ_r remain positive at those frequencies. To overcome this limitation, the ROD structure on the backside is also designed using the tri-section step-impedance technique. This approach enables left-handed current to occur at all three resonance frequencies. The ROD structure is designed to resonate at the same frequencies as the front structure, which ensures frequency matching between the front and backside structures of the unit cell. Consequently, the electromagnetic parameters change significantly at the resonance frequencies. Because the three resonance frequencies are designed as bandstop resonance frequencies,

strong reflection occurs at those frequencies. As a result, the effective permittivity exhibits epsilon-negative (ENG) characteristics [1–6], while the retrieved effective permeability remains positive within the designed resonance bands. These electromagnetic properties enable the unit cell to behave as a metamaterial, producing much stronger reflection than conventional materials and preventing transmission at the resonance frequencies. The unit-cell structure based on the proposed design techniques is illustrated in Figure 1. In Figure 1a (left), the unit-cell structure consists of a transmission line implemented with a tri-section step-impedance technique, whose end is connected using a capacitive double interdigital (C_{DI}) structure. This section generates the total capacitive load on the structure. Two techniques are combined in this region. The first is the interdigital technique, which generates a capacitance (C_i) determined by the length and spacing of the interdigital fingers [42–44]. The second technique introduces an inner interdigital finger structure, which further increases the capacitive load and generates an additional capacitance (C_i'). These two capacitances are connected in parallel, significantly increasing the total capacitive load, expressed as $C_{DI} = C_i + C_i'$. The ROD structure on the backside, shown in Figure 1a (right), also employs the tri-section step-impedance technique to generate left-handed current circulation at all designed resonance frequencies. The overall unit-cell structure is shown in Figure 1b. At the interface between the front and backside structures, additional capacitances are generated within the substrate layer. These include the substrate capacitance (C_g) between the front structure and the ROD, and the coupling capacitance (C_f) between the two structures. Although (C_f) has only a minor effect, both capacitances contribute to the total capacitance of the unit cell, while A represents the width of the transmission line, as shown in Figure 2. If the parameters of the unit-cell structure are analyzed, as shown in Figure 3a (left), the transmission line employing the tri-section step-impedance technique [39,44] is divided into three sections with different impedance values, denoted as (Z_a), (Z_b), and (Z_c). Each section also has its own propagation constant β_a, β_b, and β_c; the physical lengths are (la), (lb), and (lc), and the electrical lengths are θ_a, θ_b, and θ_c. Therefore, the total electrical length is $\theta_T = 2(\theta_a + \theta_b + \theta_c) = 2(\beta_a l_a + \beta_b l_b + \beta_c l_c)$.

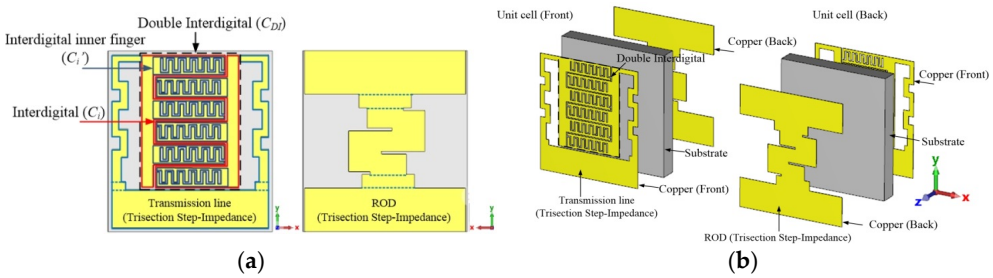


Figure 1. The configuration of multiband bandstop metamaterial unit-cell structure. (**a**) Front and back structure of the unit cell. (**b**) Material layer of the unit cell.

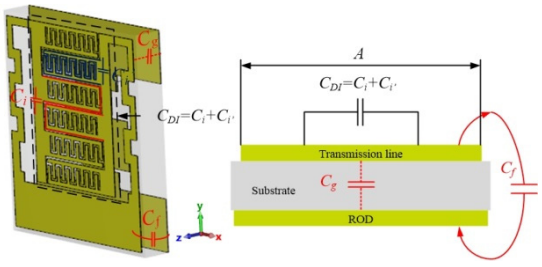


Figure 2. The overall capacitive coupling of the proposed structure multiband bandstop metamaterial unit cell.

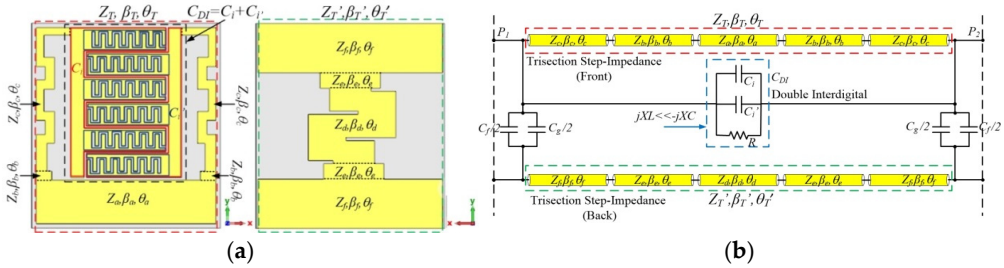


Figure 3. The configuration of the multiband bandstop metamaterial unit cell and parameters. (**a**) Tri-section step-impedance with double interdigital parameters of front and back unit-cell structure. (**b**) Equivalence circuit of multiband bandstop metamaterial unit cell.

For the ROD structure, the backside configuration employs a transmission line tri-section step-impedance technique, as illustrated in Figure 3a (right). The total electrical length is $\theta_T' = 2(\theta_d + \theta_e + \theta_f) = 2(\beta_d l_d + \beta_e l_e + \beta_f l_f)$. Based on the unit-cell structure composed of the aforementioned parameters, the equivalent circuit can be represented as shown in Figure 3b. It is observed that the front transmission line structure, particularly the double interdigital section, exhibits a condition where $jXL << -jXC$, indicating a highly capacitive behavior in this region. The parameter R represents the loss in the transmission line. Furthermore, the coupling between the front structure and the backside ROD introduces capacitive elements C_g and C_f, which are connected across the unit-cell structure. These capacitances are effectively in parallel, thereby influencing the overall capacitance of the circuit. Although the effect of C_f is relatively small, it still contributes to the total capacitive behavior. Therefore, the total capacitance C_T of the unit cell can be expressed as given in Equation (1) [44,46].

$$\begin{gathered} C_T = C_{DI} + C_g + C_f \\ C_{DI} = C_i + C_i' \\ C_g = \frac{\varepsilon_0 \varepsilon_r A}{h}, C_f = C_T - C_{DI} - C_g \end{gathered} \tag{1}$$

When

$$Ci = L_F'(\varepsilon_r + 1)[0.1(n-3) + 0.11]pF$$

$$Ci' = L_f'(\varepsilon_r + 1)[0.1(n'-3) + 0.11]pF$$

From Equation (1), n and n' represent the number of fingers of the interdigital and inner interdigital structures, respectively. L_F and L_f denote the lengths of the interdigital and inner interdigital sections, while L_F' and L_f correspond to the finger lengths of the interdigital and inner interdigital structures. It should be noted that $L_f' = L_F$.

For the tri-section step-impedance structure consisting of the front transmission line and the backside ROD configuration, the analysis characteristic impedance of each section can be calculated by input impedance Z_{ina}, Z_{inb}, Z_{inc} and Z_{ind}, Z_{ine}, Z_{inf} performed using Equation (2) when Z_a, Z_b, Z_c and Z_d, Z_e, Z_f are the characteristic impedance of the front–side transmission line sections. $Z_L = 1/\mathrm{j}\omega C_T$ is the impedance at the end of the transmission line. Z_{TF} and Z_{TB} are the frequency-dependent equivalent input impedances of the complete cascaded front- and backside tri-section transmission lines, respectively, and are not arithmetic sums of the individual section impedances.

$$Z_{inc} = Z_c \frac{Z_L + jZ_c \tan\theta_c}{Z_c + jZ_L \tan\theta_c}, Z_{inf} = Z_f \frac{Z_L' + jZ_f \tan\theta_f}{Z_f + jZ_L' \tan\theta_f}$$

$$Z_{inb} = Z_b \frac{Z_{inc} + jZ_b \tan\theta_b}{Z_b + jZ_{inc} \tan\theta_b}, Z_{ine} = Z_e \frac{Z_{\mathrm{in}f} + jZ_e \tan\theta_e}{Z_e + jZ_{inf} \tan\theta_e}$$

$$Z_{TF} = Z_{ina} = Z_a \frac{Z_{inb} + jZ_a \tan\theta_a}{Z_a + jZ_{inb} \tan\theta_a}, Z_{TB} = Z_{ind} = Z_d \frac{Z_{ine} + jZ_f \tan\theta_d}{Z_d + jZ_{ine} \tan\theta_d} \quad (2)$$

The electrical length of the transmission line at resonance frequencies θ_1, θ_2 and θ_3 corresponding to the first, second, and third resonant frequencies, respectively express in Equation (3) when impedance ratios of transmission line front and ROD back are defined as R_F and R_B, where $R_{F1} = Z_b/Z_a$, $R_{F2} = Z_c/Z_b$ and $R_{B1} = Z_e/Z_d$, $R_{B2} = Z_f/Z_e$ [39,40].

$$\theta_1 = \tan^{-1}\sqrt{\frac{R_{F1}R_{F2}}{1 + R_{F1} + R_{F2}}}$$

$$\theta_2 = \tan^{-1}\sqrt{\frac{1 + R_{F1} + R_{F1}R_{F2}}{R_{F2}}}, \quad \theta_3 = \pi/2 \quad (3)$$

From (3), the relationship between the electrical length of the transmission line and the desired resonance frequencies can be determined as shown in (4), where f_1, f_2, and f_3 denote the first, second, and third resonance frequencies, respectively.

$$\frac{f_2}{f_1} = \frac{\theta_2}{\theta_1} = \frac{\tan^{-1}\sqrt{\frac{1+R_{F1}+R_{F1}R_{F2}}{R_{F2}}}}{\tan^{-1}\sqrt{\frac{R_{F1}R_{F2}}{1+R_{F1}+R_{F2}}}}$$

$$\frac{f_3}{f_1} = \frac{\theta_3}{\theta_1} = \frac{\pi/2}{\tan^{-1}\sqrt{\frac{R_{F1}R_{F2}}{1+R_{F1}+R_{F2}}}} \quad (4)$$

The impedance response of the front and backside tri-section structures is determined by the cascaded transmission line transformations in Equation (2) together with the impedance ratios and electrical lengths defined in Equations (3) and (4), where Z_T and Z_T' and the total electrical lengths satisfy θ_T and θ_T'. When the front transmission line structure is connected with the capacitive load, the electrical lengths at the three resonance frequencies can be obtained from (5), where θ_{f1}, θ_{f2}, and θ_{f3} are the electrical lengths at resonance frequency when f_1, f_2, and f_3 are resonance frequencies. From these equations, it can be observed that the capacitive load produced by the double interdigital structure, when combined with the tri-section step-impedance transmission line, affects the electrical length at all resonance frequencies when the parameters Z_{TF} and C_T are varied. The second resonance frequency is particularly sensitive to these variations, which allows it to be controlled quasi-independently and tuned from the first and third resonance frequencies. The third resonance frequency can also be quasi-independently tuned by adjusting Z_{TF} and C_T, although its frequency shift is less sensitive compared with the second resonance. Therefore, the three resonance frequencies generated by the proposed structure can be quasi-independently tuned [41,43,46].

$$\theta_{f1} = 2\tan^{-1}\left(\frac{1}{2\pi f_1 Z_{TF} C_T}\right)$$

$$\theta_{f2} = 2\pi - 2\tan^{-1}(2\pi f_2 Z_{TF} C_T)$$

$$\theta_{f3} = 2\tan^{-1}\left(\frac{1}{2\pi f_3 Z_{TF} C_T}\right) \quad (5)$$

Equations (1)–(5) are used to design the front unit-cell structure. The resonant behavior must exhibit a bandstop resonance frequency, where the insertion loss (S_{21}) is low, and the return loss (S_{11}) approaches 0 dB. This condition produces strong reflection at the resonance frequencies. If the backside ROD is not included, the effective permittivity and

permeability remain positive at the resonance frequencies. However, when a backside ROD using the tri-section step-impedance technique is introduced and tuned to resonate at the same frequencies as the front structure, the effective parameters change significantly. In this case, the permittivity becomes epsilon-negative (ENG) and the positive permeability within the bandstop resonance frequency range, covering the designed operational bandwidth. These negative characteristics arise from the formation of a left-handed current within the unit cell. In the bandstop resonance region, the structure exhibits high reflection and low transmission, which gives the unit-cell metamaterial properties with stronger reflective behavior than conventional materials. At frequencies near but outside the resonance bands, the effective parameters return to positive values similar to those of ordinary materials. Therefore, the bandstop resonance frequency of the structure can be determined using Equation (6) [33–35,37].

$$F_{even} = \tan\theta_{Tf} - \frac{1}{\omega C_T Z_{TF}} = 0$$
$$F_{odd} = \tan\theta_{Tf} + \omega C_T Z_{TF} = 0 \quad (6)$$

When

$$\omega = 2\pi f_n \ (\text{rad/S})$$
$$\beta = \frac{2\pi f_n \sqrt{\varepsilon_{eff}}}{C}, C\ is\ speed\ of\ light\ (3\times 10^8 \text{m/S})$$
$$\theta_{Tf1} = \left(\theta_1 + \theta_{f1}\right),\ \theta_{Tf2} = \left(\theta_2 + \theta_{f2}\right),\ \theta_{Tf3} = \left(\theta_3 + \theta_{f3}\right)$$

From (6), the resonance frequencies are divided into two modes. The first is the even mode, which corresponds to the resonance frequency region for transmission, where S_{21} approaches 0 dB, and S_{11} has a low value. This region is commonly referred to as the passband. The second is the odd mode, which represents the bandstop region, where S_{21} becomes low while S_{11} approaches 0 dB.

This bandstop region is used in the design of the resonance characteristics of the unit cell. From the odd-mode or bandstop resonance analysis, the total capacitance and the tri-section impedance ratios significantly affect the total electrical length (θ_{Tf}). This electrical length is the combination of the electrical lengths of the transmission line and the double interdigital structure within the unit cell. As a result, these parameters strongly influence the control of the three bandstop resonance frequencies, allowing them to resonate at the desired frequencies and to be quasi-independently tuned, separated from one another. The design of the unit cell using (1)–(6) shows that the resonance frequencies can be controlled at 1.8 GHz, 2.6 GHz, and 3.5 GHz. After calculating S_{21} and S_{11}, the effective electromagnetic parameters ε and μ can be retrieved from the simulated S-parameters. The wave impedance z, refractive index n, and m are the integer branch index associated with the multivalued inverse-cosine function and are calculated as shown in Equation (7), where k_0 is the free-space wavenumber and d is the substrate thickness.

$$z = \pm\sqrt{\frac{(1+S_{11})^2 - S^2{}_{21}}{(1-S_{11})^2 - S^2{}_{21}}},\ e^{ik_0 nd} = \frac{S21}{1 - S11\left(\frac{z-1}{z+1}\right)}$$
$$n(f) = \frac{-jLog\left[\frac{S_{21}}{1-S_{11}\left(\frac{Z-1}{Z+1}\right)}\right] + 2\pi m}{k_0 d}$$
$$\varepsilon = \frac{n}{z},\ \mu = nz \quad (7)$$

In addition, effective permittivity becomes negative, while the effective permeability characteristic is positive over the operating bandwidth. These properties make the structure

suitable for array implementation as a reflector for antenna applications. Furthermore, increasing the capacitive load significantly enhances the slow-wave effect, which enables the physical size of the structure to be reduced to approximately $\lambda/16$. The parameters of the unit cell are illustrated in Figure 4. Based on the proposed unit-cell geometry, the corresponding capacitive and inductive components were identified. The capacitance generated by the double-interdigital structure was calculated using Equation (1). For the outer interdigital structure, C_i = 4.4 + 1[0.1(6 − 3) + 0.11)] = 1.016 pF when N = 6, l = 0.459 cm and C_i' = 4.4 + 1(0.076) [0.1(11 − 3) + 0.11] = 0.373 pF when n = 11, L_f' = 0.076 cm. Therefore, the total capacitance of the double-interdigital structure is C_{DI} = 1.389 pF. The additional capacitance generated by the overlapping regions of the front and backside structures was calculated as $C_g = 8.854 \times 10^{-12}(4.4)\ (38.7 \times 10^{-6}/1.6 \times 10^{-3}) = 0.942$ pF when A = 38.7 mm^2 and $h = 1.6 \times 10^{-3}$. The coupling capacitance was subsequently calculated as C_f = 4.688 pF; consequently, the total equivalent capacitance of the unit cell is C_T = 1.389 + 0.942 + 4.688 = 7.020 pF. The frequency-dependent equivalent inductance of the unit cell was calculated using $L_T = 1/(2\pi f)^2 C_T$. Accordingly, the equivalent inductances at 1.8 GHz, 2.6 GHz and 3.5 GHz are 1.1137 nH, 0.5338 nH and 0.2946 nH, respectively. For the front-side unit-cell structure, the initial characteristic impedance was set to 55 Ω. By applying the tri-section stepped-impedance technique to control the second- and third-order resonances, the impedances of the three sections were determined as Z_a = 100 Ω, Z_b = 90 Ω and Z_c = 20Ω. The impedance ratios of the tri-section step-impedance are $R_{F1} = Z_b/Z_a$ = 0.9 and $R_{F2} = Z_c/Z_b$ = 0.222. For the tri-section stepped-impedance ROD structure on the back side of the unit cell, the section impedances are set to Z_d = 80 Ω, and are specified as Z_e = 50 Ω and Z_f = 20 Ω. The impedance ratios of ROD are $R_{F1} = Z_e/Z_d$ = 0.625 and $R_{F2} = Z_f/Z_e$ = 0.400. The calculated values of C_T, together with the section characteristic impedances, electrical lengths, and the cascaded equivalent impedances obtained from Equation (2) and L_T, were subsequently substituted into Equations (2)–(6) to determine the resonance conditions at the three target frequencies. These electrical parameters were also used to calculate the initial width and length of each section of the proposed structure. The calculated dimensions were subsequently optimized to accurately position all three resonances at their target frequencies. The optimized dimensions remained close to the analytically calculated values and are summarized as the unit-cell parameters in Table 1.

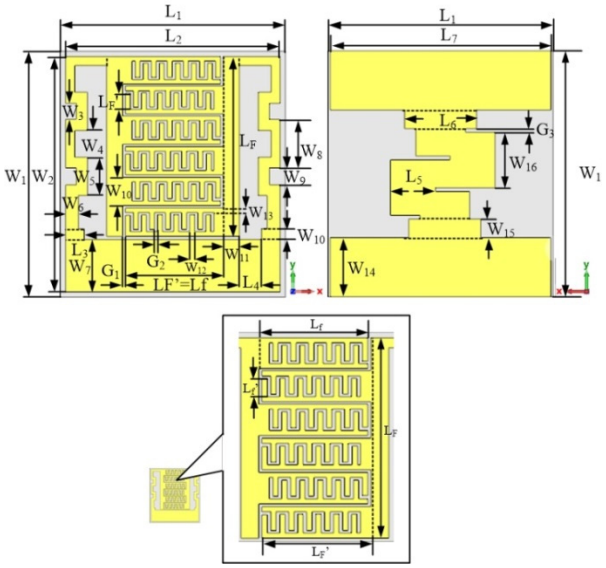


Figure 4. The proposed structure of the multiband bandstop metamaterial unit cell and parameters.

Table 1. The proposed parameters of the structure of the multiband bandstop metamaterial unit cell.

Parameters (mm)			
W_1 = 11.55 mm	W_9 = 0.79 mm	L_1 = 10.57 mm	$L_{f'}$ = 0.76 mm
W_2 = 11.05 mm	W_{10} = 0.5 mm	L_2 = 10.07 mm	L_F = 8.44 mm
W_3 = 0.75 mm	W_{11} = 0.75 mm	L_3 = 0.87 mm	$L_{F'}$ = 4.59 mm
W_4 = 1.25 mm	W_{12} = 0.23 mm	L_4 = 1.05 mm	G_1 = 0.15 mm
W_5 = 1.8 mm	W_{13} = 0.21 mm	L_5 = 2.12 mm	G_2 = 0.18 mm
W_6 = 0.6 mm	W_{14} = 2.78 mm	L_6 = 3.38 mm	G_3 = 0.55 mm
W_7 = 2.46 mm	W_{15} = 0.87 mm	L_7 = 10.37 mm	
W_8 = 2.28 mm	W_{16} = 2.61 mm	L_f = 4.59 mm	

After the design process, the proposed unit cell is simulated to evaluate the resonance frequency response together with the effective parameters of permittivity and permeability. The excitation configuration of the unit cell is illustrated in Figure 5, where port 1 is placed in front of the structure, and port 2 is placed behind the structure along the Z and $-Z$ axes. The reference planes for S_{11} and S_{21} are established precisely at the front and back outer surfaces of the unit-cell substrate at z = 0 and z = d = 1.6 mm, effectively de-embedding the 21 mm air-gap propagation paths to the waveguide ports. The distance between each port and the unit cell is approximately $\lambda/8$ of the first resonance frequency, which is about 21 mm. This distance allows electromagnetic waves to propagate from the front side to the back side of the structure. This spacing is related to the unit-cell size of $\lambda/16$, which corresponds to the distance that produces constructive reflection to enhance the phase of a connected dipole antenna. In other words, when the unit-cell size becomes smaller, the reflection and phase enhancement for the antenna become more effective. Consequently, the distance between the antenna and the reflector can be significantly reduced. The excitation conditions are then divided into electric field (E-field) and magnetic field (H-field) excitations along the X and Y axes to examine the resonance behavior of the structure. The excitation process is categorized into two cases. In the first case, the resonance of the structure is excited by an E-field propagating along the X-axis, which is modeled as a perfect electric conductor (PEC) boundary condition, while the H-field is defined along the Y-axis with a perfect magnetic conductor (PMC) boundary condition, as shown in Figure 5a. In the second case, the excitation is applied with the E-field along the Y-axis and the H-field along the X-axis, as illustrated in Figure 5b. The simulation results show that the first excitation configuration produces multiband bandstop resonance frequencies (odd mode) in the S-parameter response. These resonance bands are clearly separated from the passband resonance frequencies (even mode), as shown in Figure 6a. In contrast, the second excitation configuration cannot clearly separate the resonance frequency bands, as illustrated in Figure 6b. This occurs because the double interdigital structure and the backside ROD of the unit cell have only a minor influence on the direction of the E-field; therefore, they cannot generate the desired bandstop resonance frequencies. From these two excitation conditions, it can be explained that the double interdigital structure and the ROD exhibit strong resonance responses to the E-field propagating along the X-axis, while they have minimal influence on the H-field. This behavior indicates that the proposed structure functions as a metamaterial with directional E-field sensitivity rather than as a high-impedance surface (HIS), which typically exhibits high impedance across the entire structure and responds to E-fields along both the X and Y directions. Further simulations are conducted to investigate the control of the resonance frequencies by increasing the capacitive load generated by the interdigital fingers. The results show that the number of fingers (N) directly affects the capacitive load. When the number of fingers increases, the capacitive load also increases, causing the first, second, and third resonance frequencies to

shift toward lower frequencies. The optimal number of fingers for the interdigital structure is $N = 6$, as shown in Figure 7a. In the double interdigital structure, increasing the number of inner fingers (n) significantly increases the capacitive load, which further shifts the resonance frequencies toward lower values. The optimal number of inner fingers is $n = 11$, as illustrated in Figure 7b. The increase in capacitive load also enhances the slow-wave effect in the unit-cell structure. As a result, the electrical length becomes significantly larger than the physical length. Therefore, in order to restore the first resonance frequency to its original target frequency, the physical length of the structure must be reduced, allowing the overall structure size to be minimized to approximately $\lambda/16$ of the first resonance frequency. Although the second and third resonance frequencies also shift toward lower frequencies, they cannot be precisely tuned to the desired frequencies by capacitive loading alone.

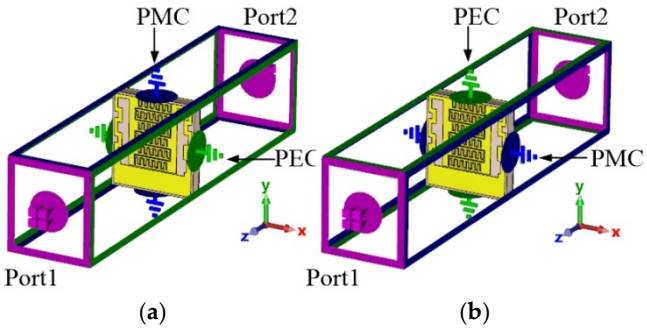


Figure 5. The simulation configurations of the structure multiband bandstop metamaterial unit cell: (**a**) PEC on X-axis and PMC on Y-axis; (**b**) PEC on Y-axis and PMC on X-axis.

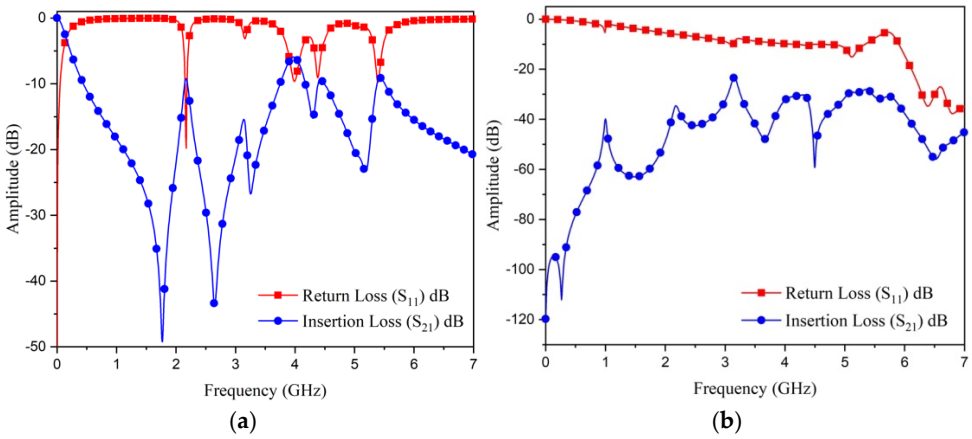
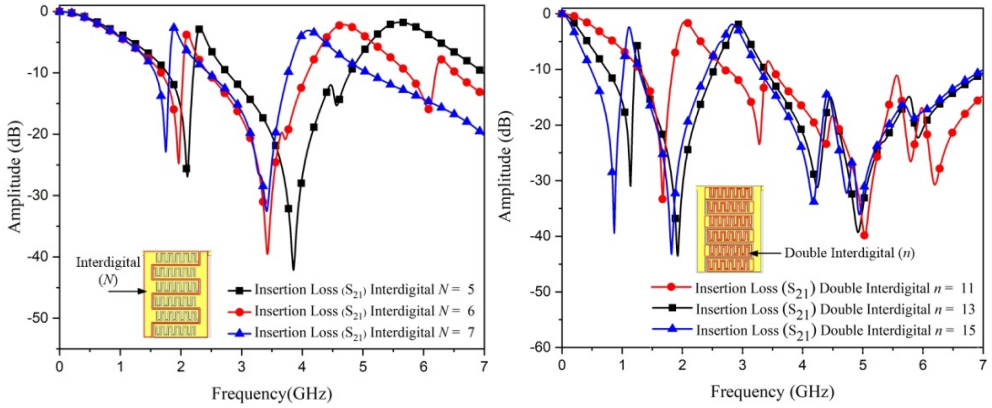


Figure 6. The simulation result of S-parameter: (**a**) PEC on X-axis and PMC on Y-axis; (**b**) PEC on Y-axis and PMC on X-axis.

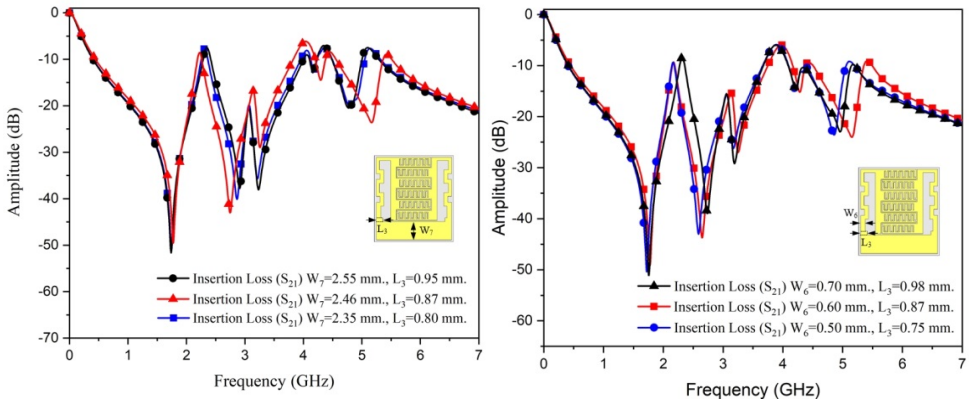
Therefore, the impedance difference in the transmission line using the tri-section step-impedance technique is introduced to control the second and third resonance frequencies together with the capacitive load. The impedance ratios are adjusted by modifying the impedances Z_a, $Z_{b,}$ and Z_c. In this design, the impedance difference between Z_a and Z_b corresponds to the parameters L_3 and W_7, while the impedance difference between Z_b and Z_c corresponds to L_3 and W_6, as shown in Figure 8a,b. The results show that the impedance ratio combined with the capacitive load strongly influences the second and third resonance frequencies, particularly the second resonance frequency, which exhibits a significant frequency shift. The third resonance frequency shifts mainly with the capacitive load, as reflected in the impedance difference. To quantitatively evaluate the resonance controllability, a normalized sensitivity matrix $S_p(f) = (\Delta f_i/f_i)/(\Delta p/p)$ is constructed, where f_i represents the resonance frequencies, and p represents the geometric design parameters.

This is summarized in Table 2. Thus, the proposed unit cell provides quasi-independent tuning capability where each structural parameter serves as a primary control knob for a specific band while secondary shifts are compensated via iterative optimization.



(**a**) (**b**)

Figure 7. The simulation result of insertion loss (S_{21}) with adjustment of the finger number of multiband bandstop metamaterial unit cell. (**a**) Finger number of interdigital. (**b**) Finger number of double interdigital.



(**a**) (**b**)

Figure 8. The simulation result of insertion loss (S_{21}) with adjustment of the tri-section step-impedance transmission line parameter of a multiband bandstop metamaterial unit cell. (**a**) Parameters W_7 and L_3. (**b**) Parameters W_6 and L_3.

Table 2. The quantitative sensitivity matrix of the proposed unit-cell resonances.

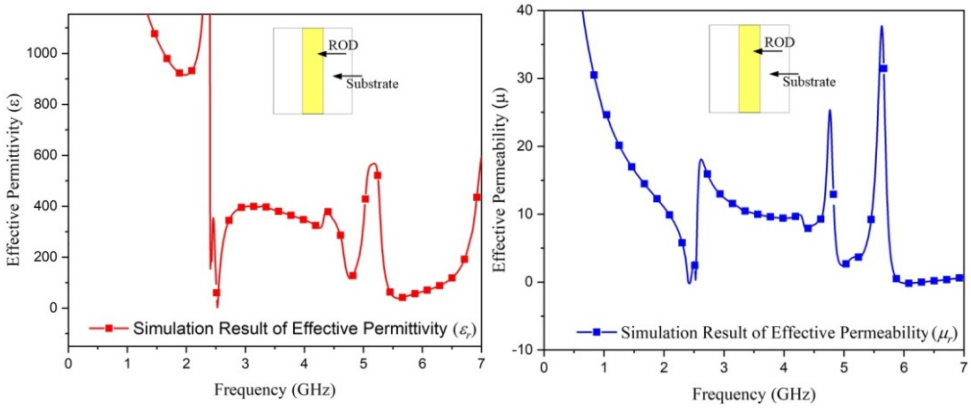
Parameter	Sensitivity at 1.8 GHz	Sensitivity at 2.6 GHz	Sensitivity at 3.5 GHz	Primary Controlled Resonance
Inner fingers (n)	−0.42	−0.21	−0.15	f_1 Capacitive Loading
Outer fingers (N)	−0.28	−0.18	−0.11	f_1 Overall Shift
Width W_7, Z_b	−0.05	−0.38	−0.08	f_2 Tri-section Impedance Ratio
Width W_6, Z_b	−0.02	−0.12	−0.31	f_3 Tri-section Impedance Ratio

This mechanism allows the three resonance frequencies to be quasi-independently tuned and separated from one another. The optimal impedance parameters are L_3 = 0.87 mm, W_6 = 0.6 mm, and W_7 = 2.46 mm. The simulation results are consistent with Equations (5) and (6), which show that the total capacitive load (C_T) and the tri-section impedance ratios strongly influence the second resonance frequency and the bandstop resonance (odd mode)

behavior. Although the proposed unit-cell structure successfully controls the separation of the bandstop resonance frequencies, it still does not exhibit metamaterial characteristics because the effective parameters ε_r and μ_r remain positive. Therefore, to obtain negative parameters, an ROD structure is introduced to generate a left-handed current within it, as reported in previous studies [11–15].

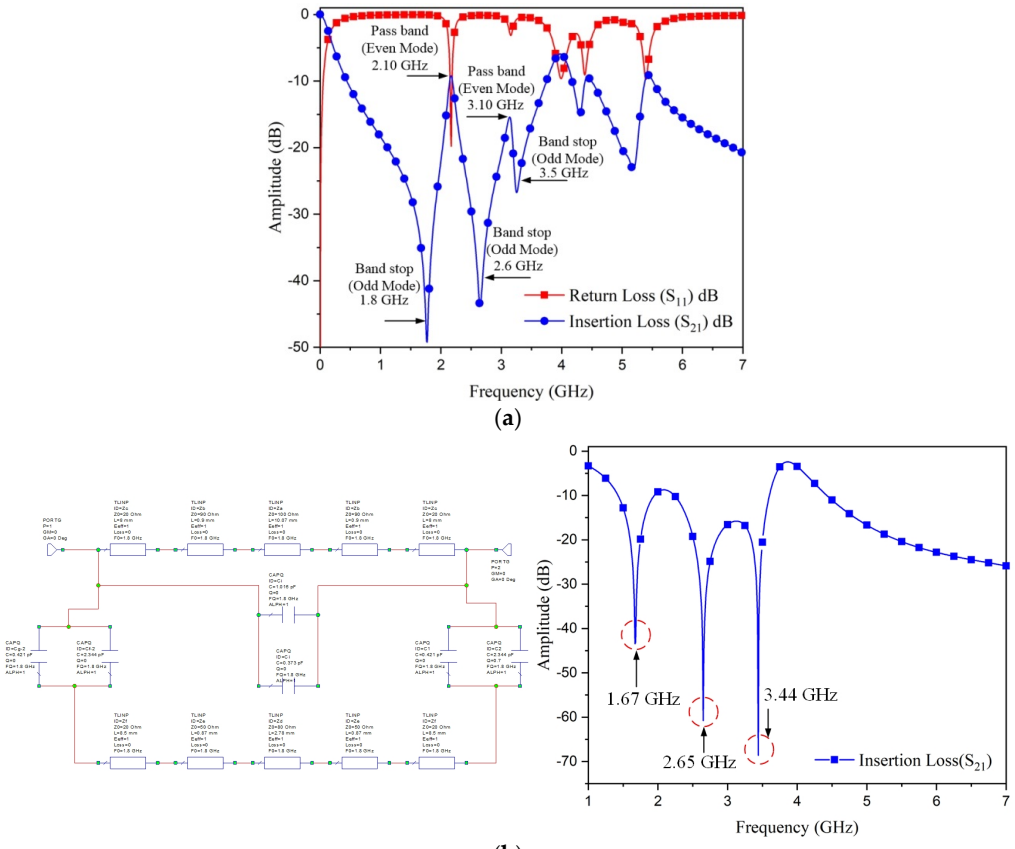
However, when a conventional ROD with a standard transmission line structure is used, it cannot produce negative resonance characteristics at all three resonance frequencies. Instead, it only reduces the coefficient near the first resonance frequency, while the second and third resonance frequencies remain unaffected. This occurs because the conventional ROD structure only supports left-handed current circulation at the first resonance frequency and cannot effectively control current circulation at the second and third resonance frequencies. As a result, both effective parameters remain positive at those frequencies. The corresponding simulation results are shown in Figure 9a,b. To achieve a negative permittivity and positive permeability, the backside ROD is redesigned so that its resonance frequencies match those of the front structure. In this work, the ROD is designed using the tri-section step-impedance technique, which uses impedance differences to control the resonance frequencies to coincide with those of the front structure. This matching between the front and backside structures at the same three resonance frequencies produces negative permittivity (ENG) and positive permeability characteristics, allowing the unit cell to exhibit metamaterial behavior and provide stronger reflection than conventional materials. After applying the proposed design techniques, the simulation of the unit cell shows bandstop resonance frequencies (odd mode) at 1.8 GHz, 2.6 GHz, and 3.5 GHz, which correspond to the desired operating frequencies. In addition, passband resonance frequencies (even mode) appear at 2.10 GHz and 3.10 GHz, as illustrated in Figure 10. To evaluate the equivalent circuit of the unit-cell structure, a performance simulation was conducted using the design parameters to verify the integration of the double-interdigital technique with the tri-section stepped impedance. The simulation results demonstrate resonances in close agreement with the desired frequency bands, exhibiting bandstop characteristics at 1.67 GHz, 2.65 GHz, and 3.44 GHz. These results confirm the accuracy of the proposed equivalent circuit and the design process described in the previous section, as shown in Figure 10b. The extracted effective parameters of permittivity and permeability show that, within the bandstop resonance frequencies, permittivity exhibits negative characteristics, while permeability shows positive characteristics. At frequencies outside the resonance bands, both parameters remain positive, as illustrated in Figure 11a. Specifically, the negative permittivity values occur as follows: at 1.8 GHz, permittivity reaches -629 and covers the frequency range 1.5–2.1 GHz; at 2.6 GHz, permittivity reaches -343.17 and covers the frequency range 2.55–3.1 GHz; and at 3.5 GHz, permittivity reaches -21.62 and covers the frequency range 3.2–3.7 GHz, as illustrated in Figure 11b. For the permeability parameter, characteristics appear at the resonance frequencies as follows: 6.288 at 1.8 GHz, 2.63 at 2.6 GHz, and 5.83 at 3.5 GHz, as illustrated in Figure 11c. These results confirm that positive permeability behavior occurs within the resonance frequency regions. Further simulations are conducted to observe the E-field and H-field responses of the unit-cell structure. When the E-field propagates along the X-axis and the H-field propagates along the Y-axis, the following behaviors are observed. In Figure 12a, the first resonance frequency (1.8 GHz) shows strong E-field responses along the transmission line, double interdigital structure, and the backside ROD, resulting in resonance at this frequency together with negative ε_r and positive permeability μ_r characteristics. At the second resonance frequency (2.6 GHz), as shown in Figure 12b, the E-field response becomes significantly stronger in the transmission line and double interdigital structure, even stronger than at the first resonance

frequency. This occurs because the capacitive load and the total impedance of the unit cell strongly influence the control of the second resonance frequency, as described in (5)–(6).



(**a**) (**b**)

Figure 9. The simulation result of effective permittivity and permeability in a conventional ROD structure. (**a**) Parameter W_7 and L_3. (**b**) Parameter W_6 and L_3.



(**a**)

(**b**)

Figure 10. The simulation result S-parameter of a multiband bandstop metamaterial unit cell under PEC/PMC boundary conditions, (**a**) showing even-mode (pass bands) and odd-mode (bandstop) resonance frequencies at 1.8 GHz, 2.6 GHz, and 3.5 GHz. (**b**) Simulation results of insertion loss (S_{21}) from equivalence circuit.

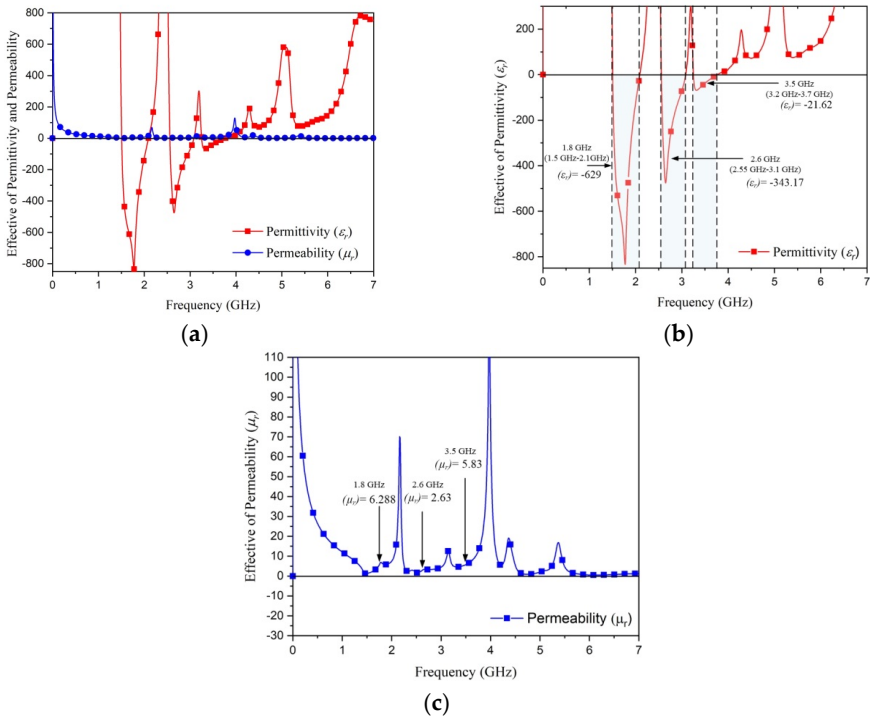


Figure 11. The simulation result of effective permittivity and permeability. (**a**) Total effective permittivity and permeability at resonance frequency. (**b**) Effective permittivity. (**c**) Effective permeability.

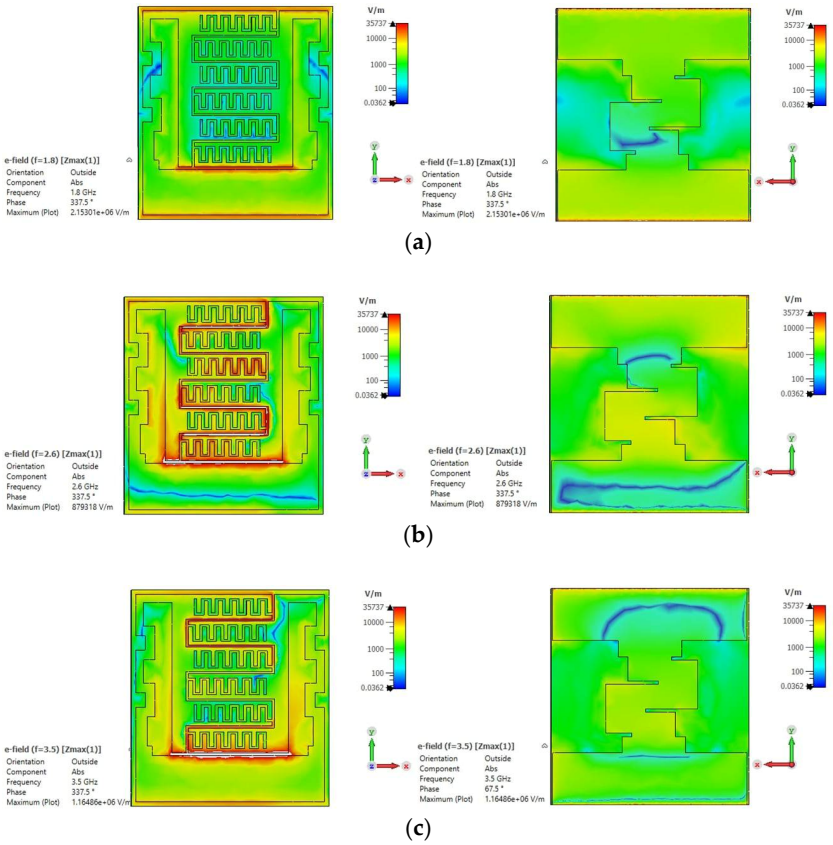


Figure 12. Simulated E-field distributions on the front and back structures of the proposed unit cell at: (**a**) 1.8 GHz; (**b**) 2.6 GHz; (**c**) 3.5 GHz.

In addition, the backside ROD also responds at this frequency, producing resonance and the corresponding negative permittivity and positive permeability characteristics. At

the third resonance frequency (3.5 GHz), shown in Figure 12c, the E-field response appears mainly in the double interdigital structure and the transmission line. The response is stronger than at the first resonance frequency but weaker than at the second resonance frequency. The ROD structure also responds to this resonance frequency, indicating that the capacitive load together with the total impedance of the transmission line continues to influence the control of this resonance frequency. In contrast, the H-field response, shown in Figure 13a–c, has only a minor influence on the unit-cell structure across all resonance frequencies. The simulated surface current distribution further confirms the resonance behavior. At 1.8 GHz, the current flows along the transmission line and the double interdigital structure, while a left-handed current circulation appears on the backside of the ROD, as shown in Figure 14a. At 2.6 GHz, strong current concentrations occur on the double interdigital structure and transmission line, and the ROD also exhibits left-handed current circulation, as illustrated in Figure 14b. At 3.5 GHz, shown in Figure 14c, a strong current distribution is observed again on the double interdigital structure, while the ROD exhibits left-handed current behavior similar to the previous two resonance frequencies. From Figures 12–14, it is clearly observed that the three resonance frequencies can be quasi-independently tuned by the capacitive load generated by the double interdigital technique together with the impedance difference in the transmission line using the tri-section step-impedance technique.

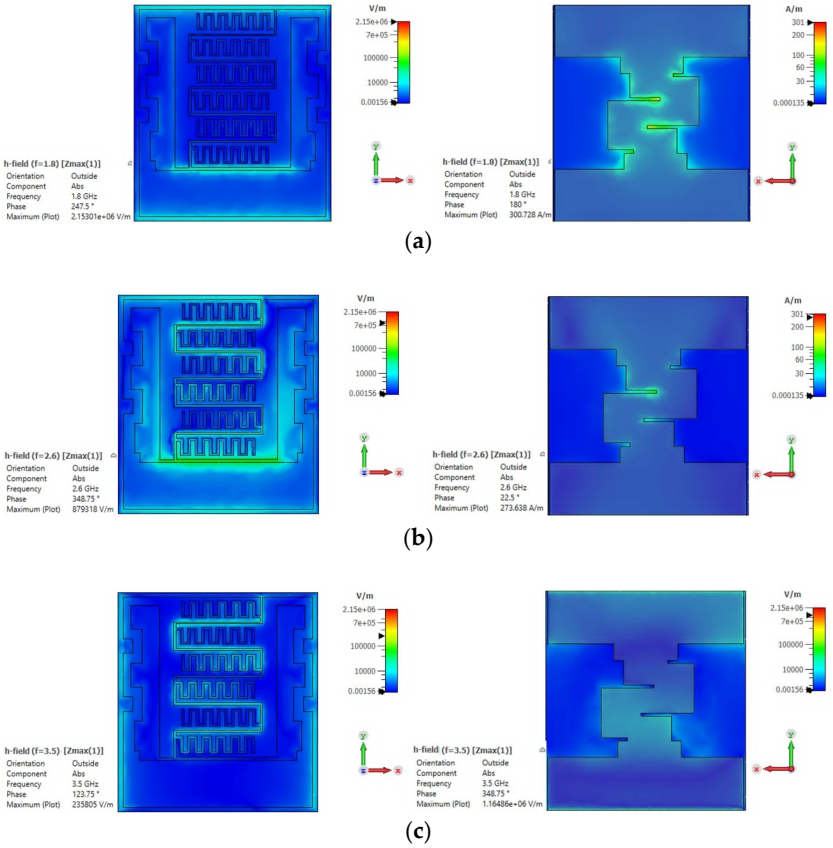


Figure 13. The simulation result of the H-field at the resonance frequency in the multiband bandstop metamaterial unit-cell front and back structure: (**a**) 1.8 GHz; (**b**) 2.6 GHz; (**c**) 3.5 GHz.

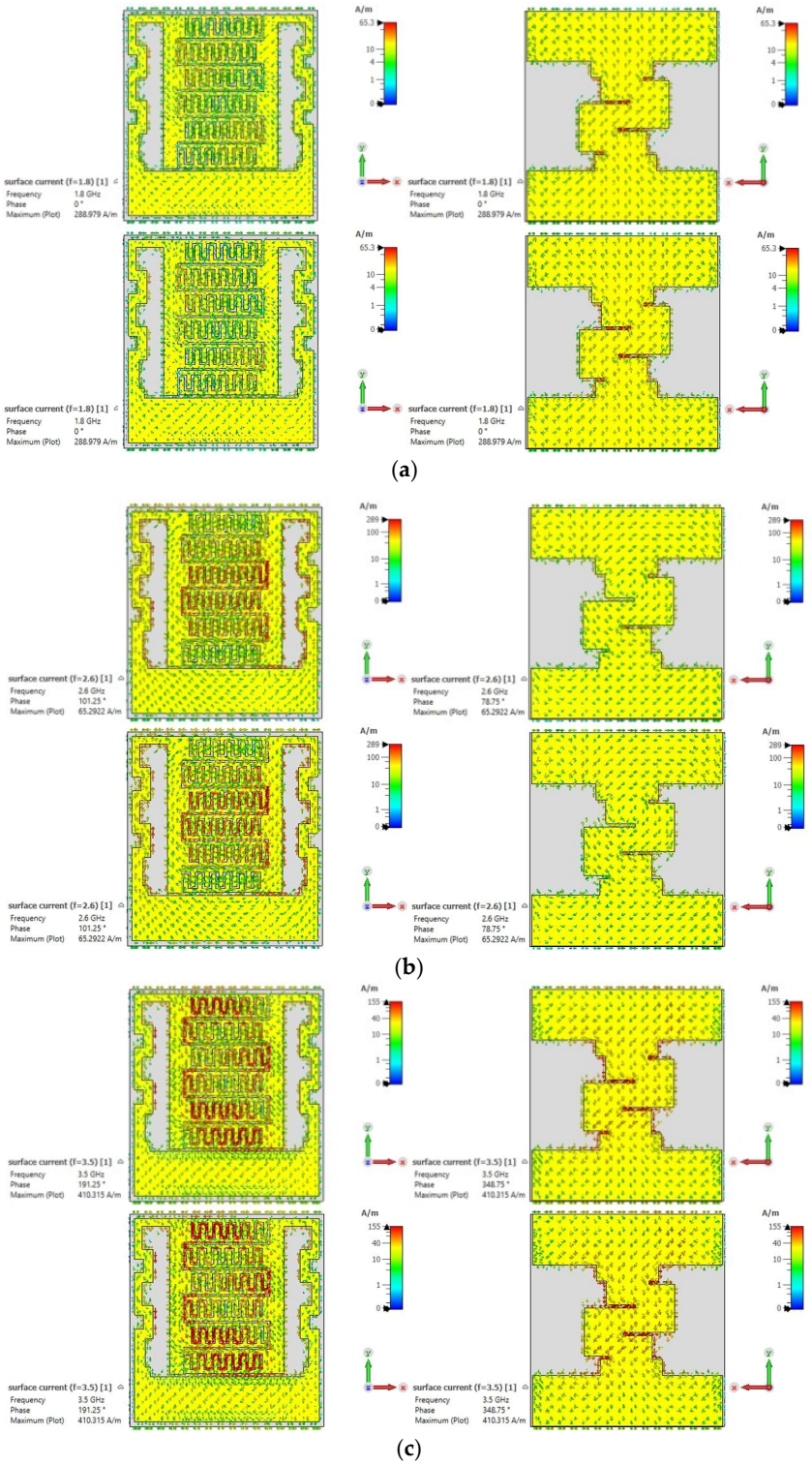


Figure 14. The simulation result of current density at resonance frequency in multiband bandstop metamaterial unit-cell front and back structure: (**a**) 1.8 GHz; (**b**) 2.6 GHz; (**c**) 3.5 GHz.

The double interdigital structure mainly responds to the E-field along the X-axis, which corresponds to the current direction of the dipole antenna used in this work, while the response to the H-field is minimal. Furthermore, the ROD designed with the tri-section step-impedance technique provides resonance matching with the front structure, producing left-handed current at all resonance frequencies, which leads to negative ε_r and positive μ_r permeability characteristics. For comparison, the proposed unit cell is compared with a conventional open-loop resonator structure that uses a standard transmission line ROD.

In that design, the resonance frequency at 1.8 GHz requires a structure length of approximately $\lambda/2$, resulting in an overall unit-cell size of 33.63 mm × 33.63 mm, as shown in Figure 15a. The simulation results in Figure 15b show that the bandstop resonance occurs only at 1.8 GHz, where permittivity becomes negative, and permeability exhibits positive characteristics but only for a single resonance frequency. In contrast, the proposed unit cell has a significantly smaller electrical size of $\lambda/16$, resulting in a much more compact structure. Moreover, it supports three quasi-independently tuned resonance frequencies while maintaining the metamaterial properties at all resonance frequencies and covering the required operating bandwidth. Finally, the proposed unit cell is arranged in an array configuration to form a metamaterial reflector, which provides stronger reflection than conventional natural materials. This reflector is then integrated with an antenna to enhance the antenna gain performance, which will be presented in the next section.

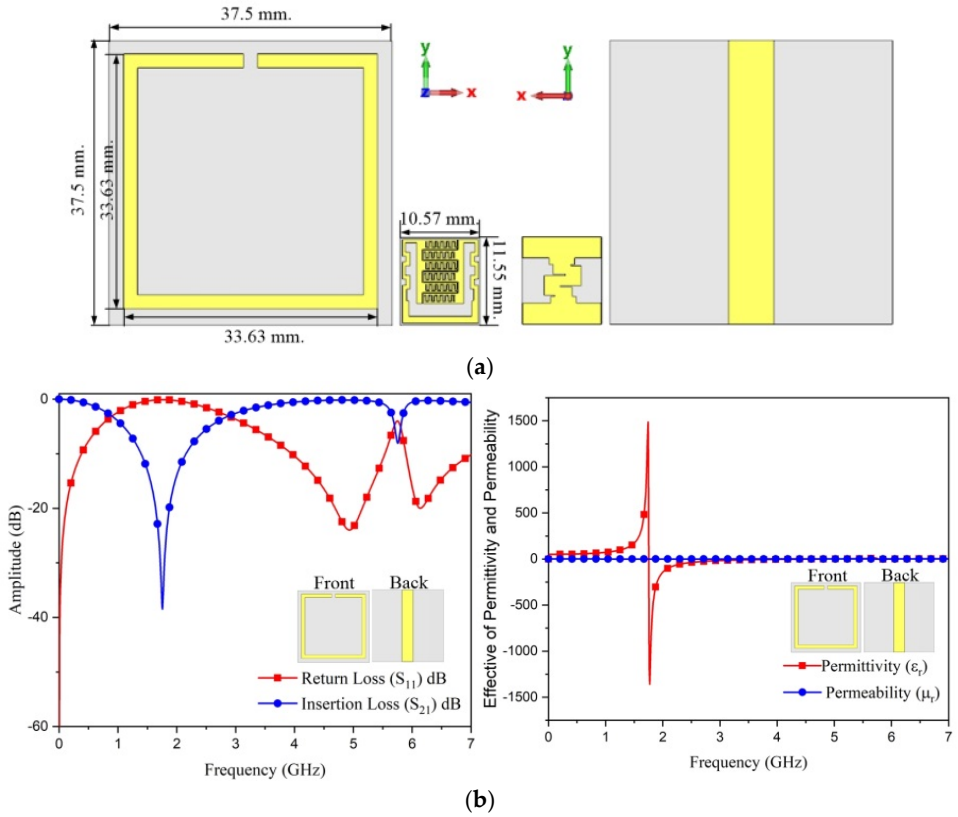


Figure 15. Comparison of the size between a typical open-loop unit cell and a multiband bandstop metamaterial unit cell and properties. (**a**) Comparison of dimensions of the unit cell. (**b**) Simulation of S-parameters and effective results.

2.2. Design of Array Unit Cell for Multibandstop Metamaterial Reflector

After the proposed unit cell is designed to exhibit multiband frequency responses, extremely compact size, and enhanced reflection characteristics compared with a conventional array configuration. The array structure serves as a reflector for antennas in order to evaluate the performance of antenna gain enhancement. The unit cells are arranged in a 14 × 14 array, which provides a suitable size for integration with the antenna and sufficiently covers the radiation area required for evaluating the reflector performance, as illustrated in Figure 16. The overall dimension of the metamaterial reflector is 161.7 mm × 148 mm. Three antennas are used for integration with the reflector. Each antenna is a dipole antenna designed to operate at a single resonance frequency band, corresponding to the reflector resonance frequencies of 1.8 GHz, 2.6 GHz, and 3.5 GHz. The antenna structures are illustrated in Figure 17, and the detailed parameters are listed

in Table 3. The antennas are constructed using copper tubes, connected with low-loss cables, and configured as balanced lines using a balun. The antenna ports utilize SMA-51 connectors. Simulation results show that all antennas achieve impedance matching below −10 dB, exhibit omnidirectional radiation patterns, and provide antenna gains of 2.03 dB, 2.22 dB, and 2.17 dB, respectively. The bandwidths are 280 MHz (1.65 –1.93 GHz), 570 MHz (2.31–2.95 GHz), and 800 MHz (3.15–3.95 GHz), respectively.

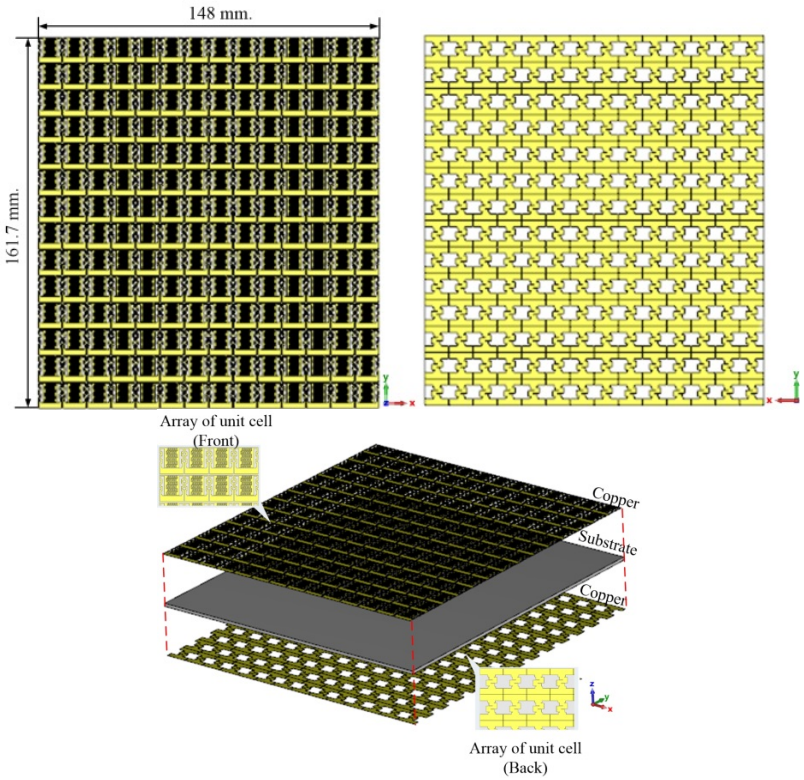


Figure 16. The reflector configuration of the array multiband bandstop unit cell with a 14 × 14 front and back structure.

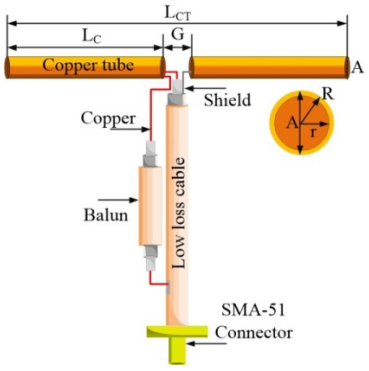


Figure 17. The single resonance frequency dipole antenna configuration.

Table 3. Parameters of the dipole antenna at resonance frequency.

Antenna Parameter	Antenna Dimension (mm)		
	1.8 GHz	**2.6 GHz**	**3.5 GHz**
L_{CT}	68.00	43.00	34.3
L_C	32.50	20.00	16.5
G	5.00	3.00	1.3
A	6	6	6
R/r	3/2.5	3/2.5	3/2.5

When integrating the antenna with the reflector, the antenna is positioned along the X-axis because the unit cell responds to the electric field, resulting in resonance along this direction. The dipole antenna carries current along its length, which corresponds to the direction of the electric field; therefore, the dipole must also be aligned along the X-axis. The antenna is placed at a distance d from the reflector. The separation distances vary for each resonance frequency and are 24.15 mm, 20.96 mm, and 17.15 mm, respectively, as shown in Figure 18a. The distance between the antenna and the reflector is less than $\lambda/4$. Since the unit-cell size is approximately $\lambda/16$, the reflector effectively interacts with the backward radiation of the antenna. The reflected waves are received and stored by the reflector, which then generates electromagnetic waves at the corresponding frequency toward the 0-degree direction, reinforcing the phase of the forward-propagating wave. As a result, the antenna gain increases significantly compared with conventional reflectors made from ordinary materials.

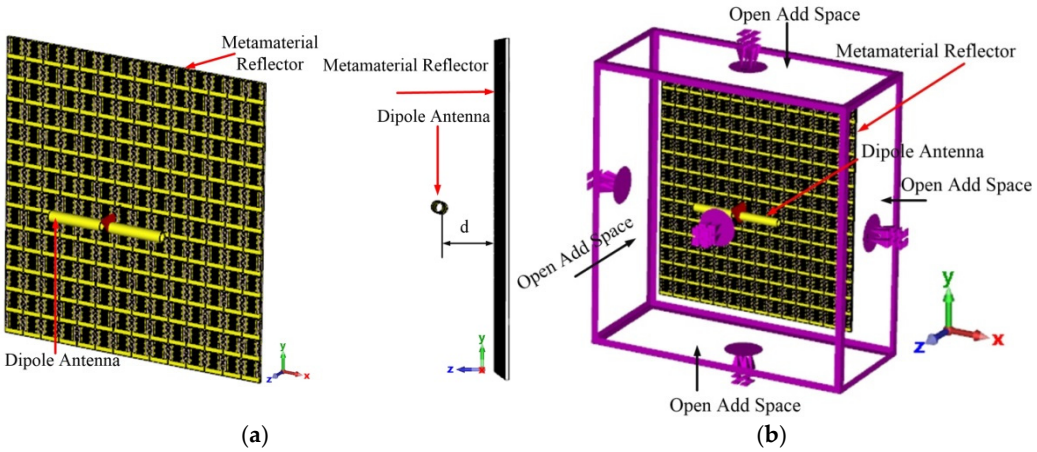


Figure 18. The proposed multiband bandstop reflector with dipole antenna. (**a**) Configuration of the multiband bandstop reflector connected with a dipole antenna. (**b**) Boundary condition setting of the multiband bandstop reflector connected with a dipole antenna for simulation.

This improvement is associated with the epsilon-negative effective permittivity, together with positive effective permeability of the proposed structure, allowing the antenna reflector spacing to be significantly reduced. During the simulation, the surrounding region of the antenna and reflector is defined as air (open add space), as illustrated in Figure 18b. The simulation results show that the antenna reflector system maintains impedance matching below -10 dB at all resonance frequencies. The bandwidth at 1.8 GHz is 1.65–2.05 GHz (400 MHz); at 2.6 GHz, the bandwidth is 2.35–2.91 GHz (560 MHz); and at 3.5 GHz, the bandwidth is 3.15–4.00 GHz (850 MHz), as illustrated in Figure 19. The simulated antenna gains are 8.23 dB at 1.8 GHz with radiation directed at 0°, 8.19 dB at 2.6 GHz with radiation at 2°, and 8.21 dB at 3.5 GHz with radiation at 0°, as shown in Figure 20. These results indicate that the antenna gain at the three resonance frequencies is significantly higher than that obtained using conventional reflectors. For comparison, conventional reflectors integrated with antennas of the same type and frequency typically provide antenna gains at the resonance frequency are 6.41 dB, 5.23 dB, and 5.78 dB, respectively, as shown by the simulation results in Figure 21, and require an antenna reflector spacing of approximately $\lambda/4$, which is larger than that required for the metamaterial reflector. The gain simulation further confirms that the antenna gain significantly increases at the designed resonance frequencies, while lower gain values appear at other frequencies, as illustrated in Figure 22.

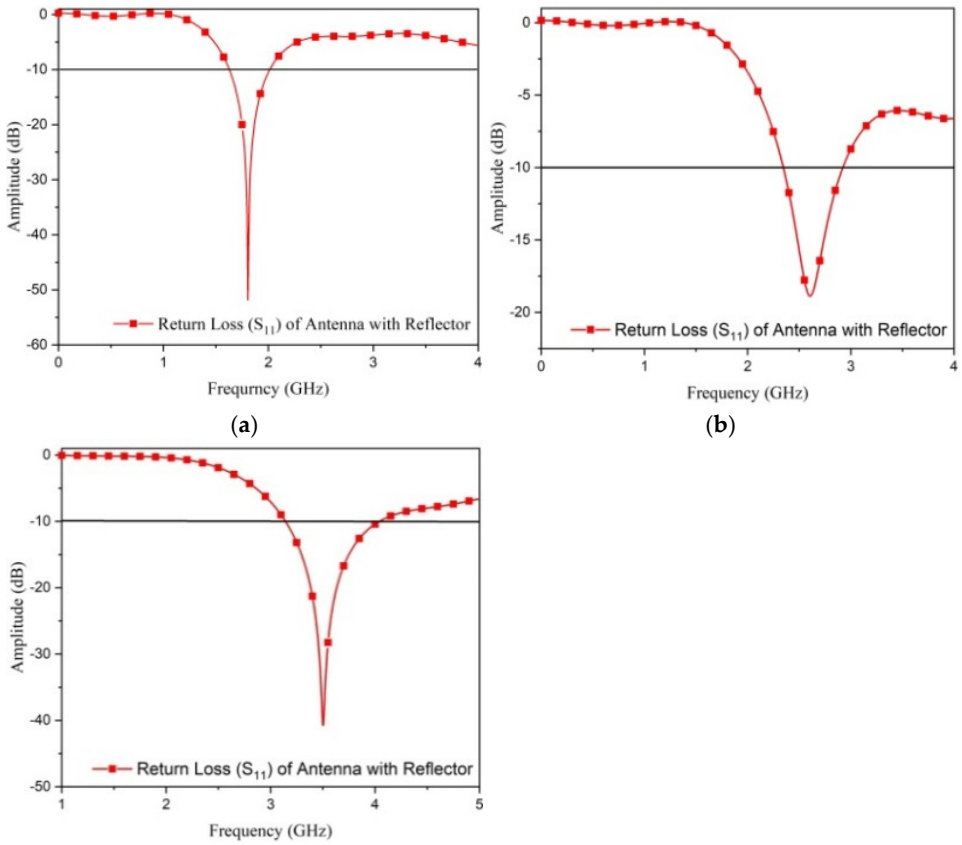


Figure 19. The simulation results of return loss at resonance frequency: (**a**) 1.8 GHz; (**b**) 2.6 GHz; (**c**) 3.5 GHz.

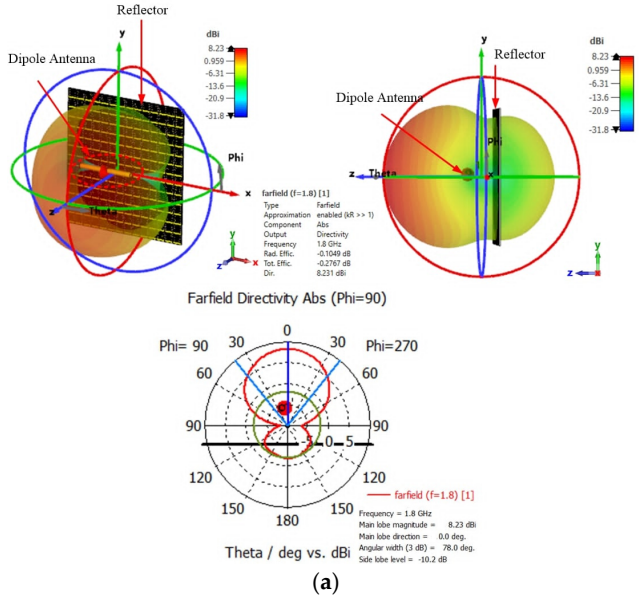
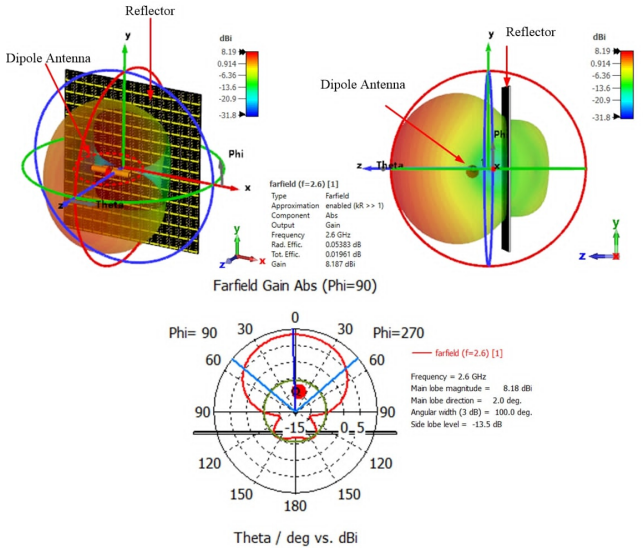
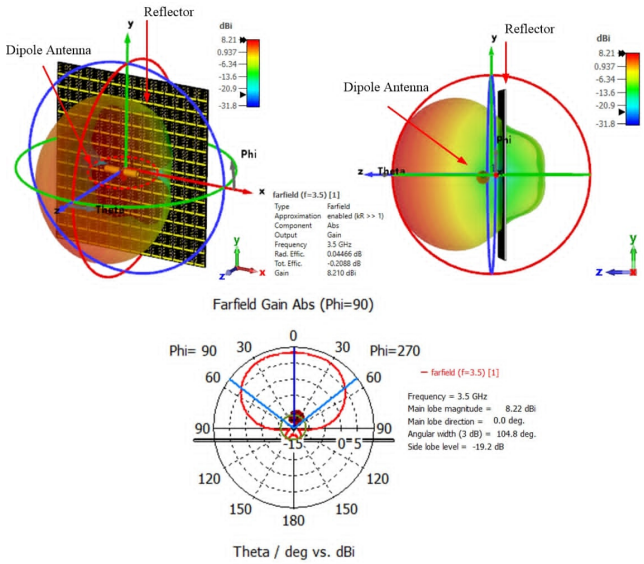


Figure 20. *Cont.*

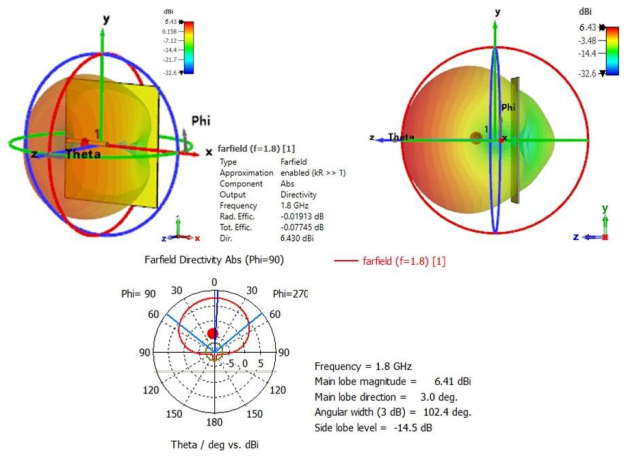


(**b**)



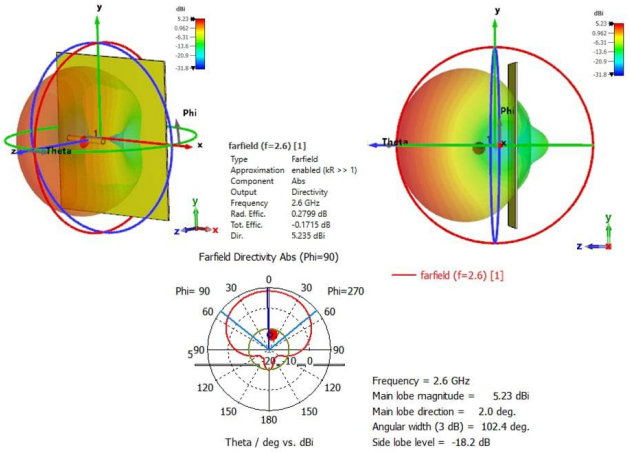
(**c**)

Figure 20. The simulation results of the radiation pattern from a dipole antenna with a metamaterial reflector at resonance frequency: (**a**) 1.8 GHz; (**b**) 2.6 GHz; (**c**) 3.5 GHz.

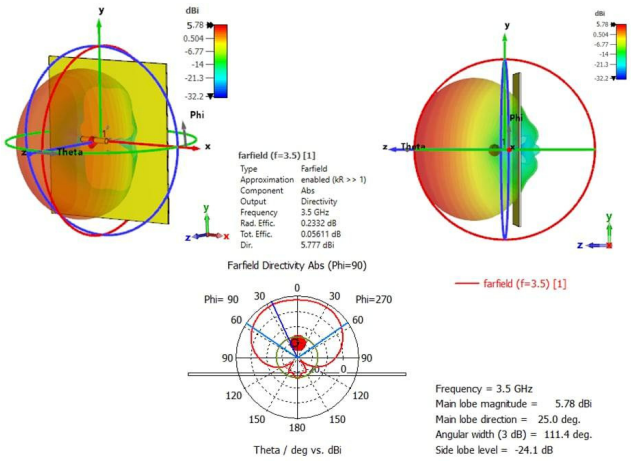


(**a**)

Figure 21. *Cont.*



(**b**)



(**c**)

Figure 21. The simulation results of the radiation pattern from a dipole antenna with a conventional reflector at resonance frequency: (**a**) 1.8 GHz; (**b**) 2.6 GHz; (**c**) 3.5 GHz.

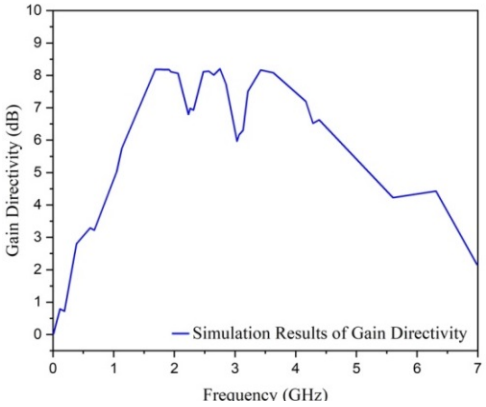


Figure 22. The simulation result of gain.

The simulation results of the dipole antenna integrated with the metamaterial reflector indicate that when the effective permittivity becomes negative and the effective permeability remains positive, the antenna gain increases substantially—from approximately 2 dB to about 8 dB. Furthermore, the unit-cell design employing the double interdigital technique combined with tri-section step-impedance enables the structure to produce three resonance frequencies while maintaining a compact size of approximately $\lambda/16$. When the unit cells are arranged in an array to function as a reflector, the overall structure becomes signifi-

cantly more compact, and the spacing between the antenna and reflector can be reduced to approximately $\lambda/8$. This reduction occurs because the unit-cell size directly influences the reflection behavior required for phase reinforcement in front of the antenna; smaller unit-cell dimensions allow the antenna-reflector distance to be reduced accordingly.

3. Measurement and Results

The fabrication of the metamaterial reflector and dipole antenna was obtained from the design and simulation, together with the experimental measurement of their performance. The metamaterial reflector structure is fabricated on an FR-4 printed circuit board using a milling machine. The overall dimensions of the structure are 148 mm $\times$ 161.7 mm. The front and back views of the fabricated structure are shown in Figure 23a.

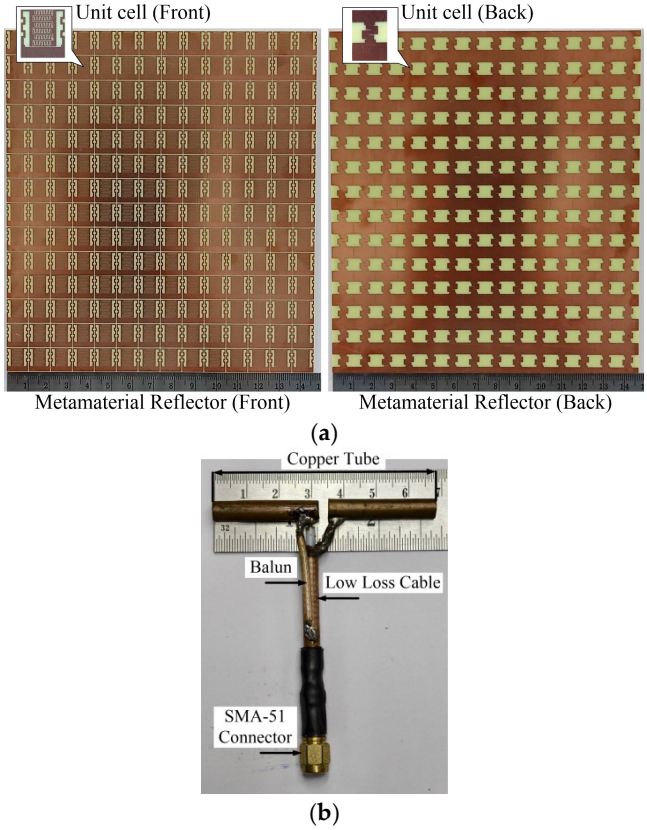


Figure 23. The prototype metamaterial and dipole antenna. (**a**) Structure of multiband bandstop metamaterial reflector front and back. (**b**) Structure of dipole antenna.

For the dipole antenna design, antennas with single-frequency resonance characteristics are implemented to operate at 1.8 GHz, 2.6 GHz, and 3.5 GHz, which correspond to the operating frequencies of the reflector. The antenna structure uses a copper tube connected to a low-loss RG-45 feeding line, and a $\lambda/4$ balun at the resonance frequency is employed to ensure that the antenna operates as a balanced line. The measured results show that the antenna at all resonance frequencies has an impedance matching lower than -10 dB and exhibits an omnidirectional radiation pattern. The measured antenna gains are 1.96 dB, 2.13 dB, and 2.06 dB, respectively. The structure of the dipole antenna is illustrated in Figure 23b. When the antenna is positioned in front of the reflector, the distance between the antenna and the reflector is approximately $\lambda/8$ at the resonance frequency. The separation distances between the antenna and the reflector are 24.15 mm, 20.96 mm, and 17.15 mm, respectively, which are the same as those used in the simulation. The dipole antenna is positioned along the X-axis. The measurement is carried out in a

chamber room, as shown in Figure 24. The measurement results show that at 1.8 GHz, the impedance matching is lower than −10 dB, with a bandwidth of 460 MHz (1.67–2.13 GHz). At 2.6 GHz, the impedance matching is also lower than −10 dB, with a bandwidth of 350 MHz (2.38–2.73 GHz). At 3.5 GHz, the impedance matching is lower than −10 dB, with a bandwidth of 700 MHz (3.06 GHz–3.76 GHz), respectively, as shown in Figure 25a–c. These results are generally consistent with the simulation results, although a slight deviation occurs at 3.5 GHz, which is the highest operating frequency. However, the obtained bandwidth still covers the required operating frequency range. The measured radiation patterns and antenna gains compare with the simulation results of radiation pattern and antenna gain, as shown in Figure 26. At 1.8 GHz, the measured gains in the co-polarized XZ and YZ planes were 7.74 and 7.62 dB, respectively. At 2.6 GHz, the corresponding gains were 7.86 and 7.84 dB. At 3.5 GHz, the measured gains were 7.63 and 7.71 dB, respectively; the measured results show good agreement with the simulated results.

For the cross-polarized XZ and cross-polarized YZ planes, the radiation levels at all resonance frequencies are very low, as shown in Figure 26a–c. From the measurement results, it can be observed that the metamaterial reflector connected to the dipole antenna significantly improves the antenna gain compared with a conventional reflector, which typically provides a gain of about 5 dB–6 dB at the resonance frequencies in the co-polarized XZ and co-polarized YZ planes. In contrast, the radiation levels in the cross-polarized XZ and cross-polarized YZ planes are very low and are not suitable for practical use. The proposed metamaterial reflector, designed to enhance the antenna gain as described above, can be further compared with previously reported studies in terms of characteristics and performance. The comparison results are summarized in Table 4.

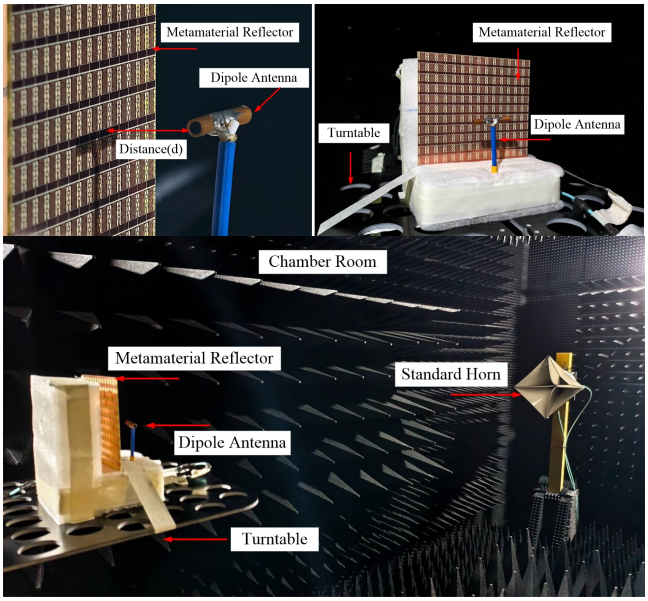


Figure 24. The measurement configuration of a multistopband metamaterial reflector connected with a dipole antenna in the chamber room.

As summarized in Table 4, the proposed reflector supports three controllable unit-cell resonances. Within these resonant bands, the effective permittivity becomes negative, demonstrating epsilon-negative (ENG) metamaterial characteristics suitable for antenna-reflector applications. The proposed unit cell is more compact than those reported in the compared studies, with an electrical size as small as $\lambda/16$ at the same operating frequency. Consequently, when the unit cells are arranged in an array, the overall dimensions of the antenna reflector can be substantially reduced. Despite its compact size, the proposed

reflector maintains high reflection efficiency, and the measured results demonstrate an antenna gain approaching 8 dB at all three resonant frequencies. Therefore, compared with the existing designs summarized in Table 4, the proposed reflector provides a smaller unit-cell and overall reflector size, high gain performance, and triple-band operation.

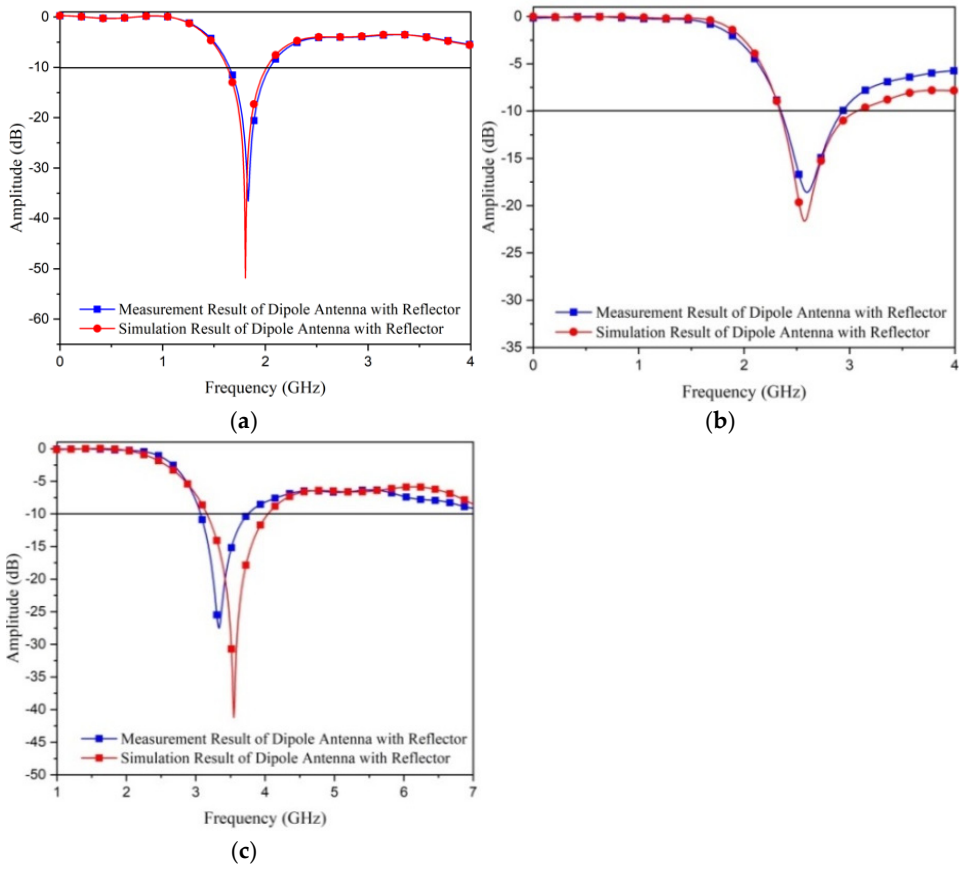


Figure 25. The comparison between simulation and measurement results of return loss (S_{11}): (**a**) 1.8 GHz; (**b**) 2.6 GHz; (**c**) 3.5 GHz.

Table 4. Performance comparison with reported single negative SNG ($\varepsilon < 0$ AND/OR $\mu \leq 0$) metamaterial resonators from the literature.

Reference Number	No. of Bands (Structure Shaped)	Freq. (GHz)	Unit-Cell Size (mm^3)	Overall Size (mm^3)	No. of Unit-Cell Array	Measurement Gain (dB)	Type of Applications
[3]	2 (Dual-band, Cross Circular Loop Resonator)	2.64 and 2.85	12 × 12	12 × 12	-	-	Reflector
[5]	1 (Random Spatial Distribution in 3D Volume)	2.965	6.7 × 6.7 × 0.254	6.7 × 6.7 × 0.254	8 × 8	-	Electromagnetic Absorbers and EMI Shielding
[8]	2 (Asymmetric Triangular Split-Ring ELC Resonator)	8.2 and 12	8 × 8 × 0.8	-	-	-	absorber
[15]	1 (CCSRRs)	3–8.4	4 × 4 × 1.52	28 × 34 × 1.52	-	6.9	Antenna
[20]	3 (Meander Line Uniplanar EBG)	2.29, 3.78 and 5.2	7 × 7 × 1.575	-	11 × 7	3.50, 4.20, 6.19	Gain enhancement

Table 4. *Cont.*

Reference Number	No. of Bands (Structure Shaped)	Freq. (GHz)	Unit-Cell Size (mm^3)	Overall Size (mm^3)	No. of Unit-Cell Array	Measurement Gain (dB)	Type of Applications
[30]	2 (Jerusalem with Interdigital)	1.8 and 5.5	30 × 30 × 0.762	150 × 150 × 0.762	5 × 5	8.23 and 8.30	Reflector
[32]	3 (Interdigital)	1.8, 3.7 and 5.2	11.53 × 10.77 × 1.6	92.24 × 86.16 × 1.6	8 × 8	3.67, 3.16 and 3.42	FSS director
[46]	3 (ICPW with Meander Line)	1.8, 3.7 and 5.8	14 × 14 × 1.6	98 × 98 × 1.6	7 × 7	5.73, 8.19 and 7.79	Director and reflector
[47]	1 (Rectangular Patches)	5	6.5 × 10 × 3.2	39 × 40 × 3.2	6 × 4	6.52	Reflector
[48]	1 (Square Patches)	2.45	25 × 25 × 3.048	125 × 100 × 3.048	5 × 3	Excess of 10	Reflector
Proposed metamaterial	3 (Multiband Bandstop Metamaterial)	1.8, 2.6 and 3.5	10.57 × 11.55 × 1.6	148 × 161.7 × 1.6	14 × 14	7.74, 7.86 and 7.63	Reflector

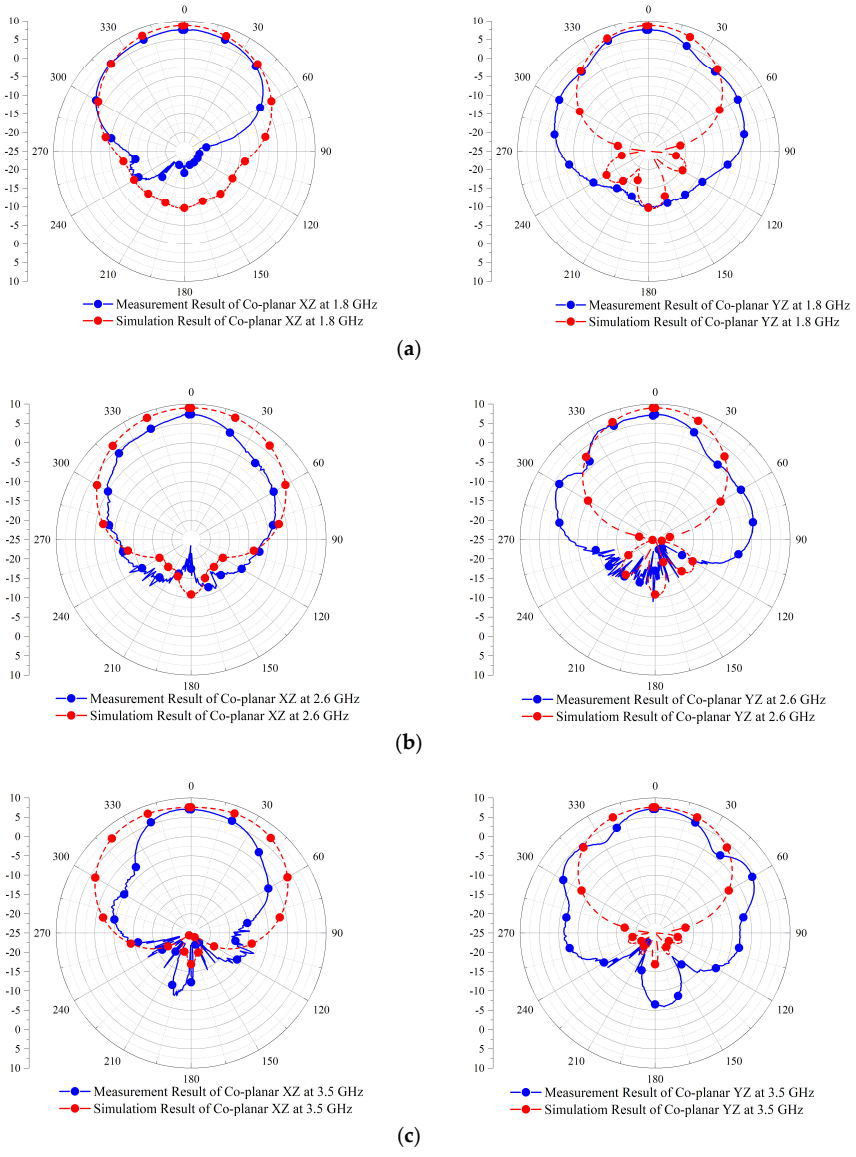


Figure 26. The comparison between measurement and simulation results of the radiation pattern in the XZ plane and YZ plane: (**a**) 1.8 GHz, (**b**) 2.6 GHz, (**c**) 3.5 GHz.

4. Conclusions

The design of a multiband bandstop metamaterial reflector using the double interdigital with tri-section step-impedance technique has been proposed. The unit cell enables quasi-independently tuned control of three bandstop resonance frequencies, allowing the resonances to occur separately at 1.8 GHz, 2.6 GHz, and 3.5 GHz, respectively. The ability to quasi-independently tune and control the resonance frequencies results from the combination of the double interdigital technique and the tri-section step-impedance structure. The capacitive load generated by the double interdigital structure, which is connected at the end of the transmission line, affects the shifting of all resonance frequencies. Therefore, the resonance frequencies can be adjusted by increasing or decreasing the capacitive load. However, capacitive loading alone does not fully separate the three resonance frequencies. To achieve independent control of each resonance frequency, the transmission line must incorporate impedance variation using the tri-section step-impedance technique. As a result, the proposed structure enables the three resonance frequencies to be quasi-independently tuned. The use of the double interdigital technique significantly increases the capacitive load, which reduces the size of the unit cell to approximately $\lambda/16$, much smaller than conventional unit cells. To ensure that the unit cell exhibits metamaterial characteristics, an ROD structure is introduced on the backside to generate a left-handed current within the structure. The tri-section step-impedance technique is also applied to the ROD structure, enabling the generation of left-handed current at all three resonance frequencies. Finally, the proposed unit cell has been arranged in an array configuration to form a metamaterial reflector, and the overall reflector size has been significantly reduced due to the compact unit-cell dimensions. To evaluate the reflector performance, single-frequency dipole antennas operating at the same resonance frequencies as the reflector were employed. The original antenna gains were 2.03 dB, 2.22 dB, and 2.17 dB, respectively. The antennas were positioned in front of the reflector along the X-axis. The simulation results showed that the antenna impedance matching at all frequencies was below -10 dB, while the antenna gains increased to 8.23 dB, 8.19 dB, and 8.21 dB, respectively. The measurement results were close to the simulation, where the antenna impedance matching remained below -10 dB at all resonance frequencies, and the measured gains increased to 7.74 dB, 7.86 dB, and 7.63 dB, respectively. The demonstrated multiband operation, compact configuration, and measured antenna-gain enhancement indicate that the proposed reflector has potential for future multiband antenna applications including 5G/6G, radar, and satellite communication systems. However, system-level improvements in 5G/6G communication performance, radar detection range, and satellite transmission distance were not experimentally evaluated in this work and remain subjects for future investigation.

Author Contributions: Conceptualization, J.K. and P.C.; methodology, J.K. and P.C.; software, J.K. and P.C.; validation, P.A., J.K. and P.C.; formal analysis, J.K. and P.C.; investigation, J.K. and P.C.; resources, P.A. and N.S.; data curation, N.S.; writing—original draft preparation, J.K. and P.C.; writing—review and editing, J.K. and P.C.; visualization, N.S. and P.A.; supervision, P.A.; project administration, P.C.; funding acquisition, P.C. All authors have read and agreed to the published version of the manuscript.

Funding: This research was funded by the King Mongkut's University of Technology North Bangkok, grant number KMUTNB-FF-68-B-27.

Data Availability Statement: This research includes the original contributions offered in the article. Additional queries may be sent to the first and corresponding author.

Conflicts of Interest: The authors declare no conflicts of interest.

References

1. Caloz, C.; Itoh, T. *Electromagnetic Metamaterials: Transmission Line Theory and Microwave Applications*; Wiley: New York, NY, USA, 2006.
2. Marqués, R.; Martín, F.; Sorolla, M. *Metamaterials with Negative Parameters: Theory, Design, and Microwave Applications*; John Wiley & Sons, Inc.: Hoboken, NJ, USA, 2008.
3. Zhong, J.; Huang, Y.; Wen, G.; Sun, H.; Gordon, O.; Zhu, W. Dual-band negative permittivity metamaterial based on cross circular loop resonator with shorting stubs. *IEEE Antennas Wirel. Propag. Lett.* **2012**, *11*, 803–806. [CrossRef]
4. Sakai, O.; Nakamura, Y.; Iwai, A.; Iio, S. Negative-permittivity plasma generation in negative-permeability space with high-energy metamaterials. *Plasma Sources Sci. Technol.* **2016**, *25*, 055019. [CrossRef]
5. Machac, J. A negative permittivity metamaterial composed of planar resonators with randomly detuned resonant frequencies and randomly distributed in space. *Int. J. Microw. Wirel. Technol.* **2018**, *10*, 1028–1034. [CrossRef]
6. Hannan, S.; Islam, M.T.; Hoque, A.; Singh, M.J.; Almutairi, A.F. Design of a Novel Double Negative Metamaterial Absorber Atom for Ku and K band Applications. *Electronics* **2019**, *8*, 853. [CrossRef]
7. Venneri, F.; Costanzo, S.; Borgia, A. A Dual-Band Compact Metamaterial Absorber with Fractal Geometry. *Electronics* **2019**, *8*, 879. [CrossRef]
8. Jinpil, T.; Yunnan, J.; Jaehoon, C. A dual-band metamaterial microwave absorber. *Microw. Opt. Technol. Lett.* **2016**, *58*, 2052–2057. [CrossRef]
9. Huang, H.-F.; Li, T. A Minimized 2-D Left-Handed Material Spiral Unit Cell with Rotation Symmetry for Midrange Wireless Power Transfer. *IEEE Microw. Wirel. Compon. Lett.* **2017**, *27*, 882–884. [CrossRef]
10. Abdelkarim, M.; Bahrouni, M.; Gharsallah, A. A compact triple band antenna based on multiple split-ring resonators for wireless applications. *Electronics* **2025**, *14*, 2271. [CrossRef]
11. Hasan, M.M.; Faruque, M.R.I.; Islam, S.S.; Islam, M.T. A new compact double-negative miniaturized metamaterial for wideband operation. *Materials* **2016**, *9*, 830. [CrossRef] [PubMed]
12. Hoque, A.; Islam, M.T.; Almutairi, A.F.; Chowdhury, M.E.H. DNG Metamaterial Reflector Using SOCT Shaped Resonator for Microwave Applications. *IEEE Access* **2021**, *9*, 59148–59159. [CrossRef]
13. Hasan, M.M.; Islam, M.T.; Moniruzzaman, M.; Soliman, M.S.; Alshammari, A.S.; Sulayman, I.I.M.A.; Samsuzzaman, M.; Islam, M.S. Symmetric engineered high polarization-insensitive double negative metamaterial reflector for gain and directivity enhancement of sub-6 GHz 5G antenna. *Materials* **2022**, *15*, 5676. [CrossRef] [PubMed]
14. Alam, M.J.; Latif, S.I. Double-split rectangular dual-ring DNG metamaterial for 5G millimeter wave applications. *Electronics* **2023**, *12*, 174. [CrossRef]
15. Emadian, S.R.; Ghobadi, C. Enhanced Double Negative Metamaterial Microstrip Antenna: Bandwidth, Gain Improvement, and Size Reduction for Radar Applications. *IEEE Access* **2024**, *12*, 170079–170088. [CrossRef]
16. Channab, M.; Pirri, C.F.; Angelini, A. Funneling spontaneous emission into waveguides via epsilon-near-zero metamaterials. *Nanomaterials* **2021**, *11*, 1410. [CrossRef] [PubMed]
17. El-Nady, S.; Elsharkawy, R.R.; Afifi, A.I.; El-Hameed, A.S.A. Performance improvement of substrate integrated cavity fed dipole array antenna using ENZ metamaterial for 5G applications. *Sensors* **2022**, *22*, 125. [CrossRef] [PubMed]
18. Hasan, M.M.; Islam, M.T.; Rahim, S.K.A.; Alam, T.; Rmili, H.; Alzamil, A.; Islam, M.S.; Soliman, M.S. A compact mu-near-zero metamaterial integrated wideband high-gain MIMO antenna for 5G new radio applications. *Materials* **2023**, *16*, 1751. [CrossRef] [PubMed]
19. Li, J.; Zhao, L.; Wu, P.H. A Novel Highly Directional Antenna Array Based on Epsilon-Mu-Near-Zero (EMNZ) with Air-Gap Structure. *IEEE Trans. Antennas Propag.* **2025**, *73*, 2357–2368. [CrossRef]
20. Pandey, R.; Vishwakarma, D.K. A meander line uniplanar EBG based multiband antenna using defected ground plane for WLAN and WiMAX applications. In *Proceedings of the IEEE MTT-S International Microwave and RF Conference, Hyderabad, India, 10–12 December 2015*; IEEE: New York, NY, USA, 2015; pp. 64–67.
21. Das, G.; Sharma, A.; Gangwar, R.K.; Sharawi, M.S. Performance improvement of multiband MIMO dielectric resonator antenna system with a partially reflecting surface. *IEEE Antennas Wirel. Propag. Lett.* **2019**, *18*, 2105–2109. [CrossRef]
22. Yadav, A.; Goyal, S.; Agrawal, T.; Yadav, R.P. Multiband antenna for Bluetooth/ZigBee/Wi-Fi/WiMAX/WLAN/X-band applications: Partial ground with periodic structures and EBG. *Nat. Commun.* **2020**, *11*, 4186.
23. El May, W.; Sfar, I.; Osman, L.; Ribero, J.-M. A textile EBG-based antenna for future 5G-IoT millimeter-wave applications. *Electronics* **2021**, *10*, 154. [CrossRef]
24. Li, R.; Wu, C.; Sun, X.; Zhao, Y.; Luo, W. An EBG-based triple-band wearable antenna for WBAN applications. *Micromachines* **2022**, *13*, 1938. [CrossRef] [PubMed]
25. Mantash, M.; Kesavan, A.; Denidni, T.A. Beam-tilting endfire antenna using a single-layer FSS for 5G communication networks. *IEEE Antennas Wirel. Propag. Lett.* **2018**, *17*, 29–33. [CrossRef]

26. Dong, J.; Ma, Y.; Li, Z.; Mo, J. A miniaturized quad-stopband frequency selective surface with convoluted and interdigitated stripe based on equivalent circuit model analysis. *Micromachines* **2021**, *12*, 1027. [CrossRef] [PubMed]
27. Wang, J.; Lang, T.; Hong, Z.; Xiao, M.; Yu, J. Design and fabrication of a triple-band terahertz metamaterial absorber. *Nanomaterials* **2021**, *11*, 1110. [CrossRef] [PubMed]
28. Alsulami, Q.A.; Wageh, S.; Al-Ghamdi, A.A.; Bilal, R.M.H.; Saeed, M.A. A tunable and wearable dual-band metamaterial absorber based on polyethylene terephthalate (PET) substrate for sensing applications. *Polymers* **2022**, *14*, 4503. [CrossRef] [PubMed]
29. Jahan, M.I.; Faruque, M.R.I.; Hossain, M.B.; Abdullah, S. An ultra-thin; triple-band, incident angle-insensitive perfect metamaterial absorber. *Materials* **2023**, *16*, 1623. [CrossRef] [PubMed]
30. Kamonsin, W.; Krachodnok, P.; Chomtong, P.; Akkaraekthalin, P. Dual-Band Metamaterial Based on Jerusalem Cross Structure with Interdigital Technique for LTE and WLAN Systems. *IEEE Access* **2020**, *8*, 21565–21572. [CrossRef]
31. Milias, C.; Andersen, R.B.; Lazaridis, P.I.; Zaharis, Z.D.; Muhammad, B.; Kristensen, J.T.B.; Mihovska, A.; Hermansen, D.D.S. Miniaturized multiband metamaterial antennas with dual-band isolation enhancement. *IEEE Access* **2022**, *10*, 64952–64964. [CrossRef]
32. Chomtong, P.; Krachodnok, P.; Bandudej, K.; Akkaraekthalin, P. A multiband FSS director using aperture interdigital structure for wirelesscommunication systems. *IEEE Access* **2022**, *10*, 11206–11219. [CrossRef]
33. Chen, X.-Q.; Li, P.; Lin, H.-J.; Tong, J.-Z.; Shi, X.-W. Open loop resonator bandpass filter with wide stopband using spurlines and microstrip stubs. In *Proceedings of the 2010 International Conference on Microwave and Millimeter Wave Technology, Chengdu, China, 8–11 May 2010*; IEEE: New York, NY, USA, 2010; pp. 40–43.
34. Liu, J.; Zhu, X.; Quyen, L.N.; You, C. High-suppression three-pole tunable band-pass filter using square open-loop resonator. In *Proceedings of the 2011 IEEE International Symposium on Antennas and Propagation (APSURSI), Spokane, WA, USA, 2011*; IEEE: New York, NY, USA, 2011; pp. 3365–3368.
35. Boutejdar, A.; Bennani, S.D. Design and Fabrication of Tri-Stopband Bandstop Filters Using Cascaded and Multi-Armed Methods. *Adv. Electromagn.* **2017**, *6*, 18–24. [CrossRef]
36. Bohra, H.; Ghosh, A. Design and Analysis of Microstrip Low Pass andBandstop Filters. *Int. J. Recent Technol. Eng. (IJRTE)* **2019**, *8*, 6944–6951. [CrossRef]
37. Faisal, M.; Khalid, S.; Rehman, M.U.; Rehman, M.A. Synthesis and Design of Highly Selective Multi-Mode Dual-Band Bandstop Filter. *IEEE Access* **2021**, *9*, 43316–43323. [CrossRef]
38. Rehman, A.; Rahman, M.H.A.; Aziz, N.; Mushtaq, B. Design of Highly Selective Dual Band Band Stop Filter using Dual-Path Step Impedance Resonator. *Pak. J. Eng. Technol.* **2022**, *5*, 146–151. [CrossRef]
39. Lin, X.M.; Chu, Q.X. Design of Triple-band Bandpass Filter Using Trn-section Stepped-Impedance Resonators. In *Proceedings of the 2007 International Conference on Microwave and Millimeter Wave Technology, Guilin, China, 18–21 April 2007*; IEEE: New York, NY, USA, 2007; pp. 1–3.
40. Su, L.; Naqui, J.; Mata-Contreras, J.; Martín, F. Miniature microwave notch filters and comparators based on transmission lines loaded with stepped impedance resonators (SIRs). *Micromachines* **2016**, *7*, 1. [CrossRef] [PubMed]
41. Xu, F.; Liu, X.; Guo, H.; Wang, Y.; Mao, L. A compact dual mode BPF based on interdigital structure. In *Proceedings of the 2010 International Conference on Microwave and Millimeter Wave Technology, Chengdu, China, 8–11 May 2010*; IEEE: New York, NY, USA, 2010; pp. 1595–1597.
42. Beeresha, R.S.; Khan, A.M.; Manjunath, R.H.V. Design and optimization of interdigital capacitor. *Int. J. Res. Eng. Technol.* **2016**, *5*, 73–78. [CrossRef]
43. Meesomklin, S.; Chomtong, P.; Akkaraekthalin, P. A compact multiband BPF using step-impedance resonators with interdigital capacitors. *Radioengineering* **2016**, *25*, 258–267. [CrossRef]
44. Cheng, W.; Li, L.; Liu, G.; Xiao, Y.; Wang, Z.-Y.; Yang, J.-X. An interdigital capacitor load slot antenna with compact size. *Prog. Electromag. Res. Lett.* **2016**, *64*, 15–19. [CrossRef]
45. Kurvinen, J.; Moreno, R.M.; Lehtovuori, A.; Ala-Laurinaho, J.; Khripkov, A.; Ilvonen, J.; Wonterghem, J.V.; Viikari, V. Capacitively-loaded feed line to improve mm-wave and sub-6 GHz antenna co-existence. *IEEE Access* **2020**, *8*, 139680–139690. [CrossRef]
46. Chomtong, P.; Krachodnok, P.; Mahatthanajatuphat, C.; Somjit, N.; Akkaraekthalin, P. Dual-Mode Characteristic Base on Miniaturized Metamaterial for Multiband Operation Utilizing Double-layer Interdigital and Tri-section Step-Impedance Techniques. *IEEE Access* **2023**, *11*, 126232–126250. [CrossRef]
47. Nakamura, T.; Fukusako, T. Broadband Design of Circularly Polarized Microstrip Patch Antenna Using Artificial Ground Structure with Rectangular Unit Cells. *IEEE Trans. Antennas Propag.* **2011**, *59*, 2103–2110. [CrossRef]
48. Joubert, J.; Vardaxoglou, J.C.; Whittow, W.G.; Odendaal, J.W. CPW-Fed Cavity-Backed Slot Radiator Loaded with an AMC Reflector. *IEEE Trans. Antennas Propag.* **2012**, *60*, 735–742. [CrossRef]

Disclaimer/Publisher's Note: The statements, opinions and data contained in all publications are solely those of the individual author(s) and contributor(s) and not of MDPI and/or the editor(s). MDPI and/or the editor(s) disclaim responsibility for any injury to people or property resulting from any ideas, methods, instructions or products referred to in the content.